Collimator irradiation studies in the Argonne Advanced Photon Source at energy densities expected in next-generation storage ring light sources

J. Dooling,* M. Borland, W. Berg, J. Calvey, G. Decker, L. Emery, K. Harkay, R. Lindberg, G. Navrotksi, V. Sajaev, S. Shoaf, Y. P. Sun, K. P. Wootton, and A. Xiao

Advanced Photon Source, Argonne National Laboratory, 9700 South Cass Avenue, Argonne, Illinois 60439, USA

A. Grannan

Nuclear Science and Engineering, Argonne National Laboratory, 9700 South Cass Avenue, Argonne, Illinois 60439, USA

A. H. Lumpkin

Argonne Associate, Argonne National Laboratory, 9700 South Cass Avenue, Lemont, Illinois 60439, USA

(Received 7 May 2021; accepted 28 February 2022; published 8 April 2022)

The Advanced Photon Source (APS) team is building a fourth-generation storage ring (4GSR), replacing the present double-bend achromat lattice with a multibend achromat system thereby allowing the production of ultrabright x-ray beams. The new lattice enables a 2-order-of-magnitude reduction in horizontal beam emittance and a factor of two increase in beam current. The result is an electron beam of very high energy and power densities. Initial predictions suggest many common ultrahigh-vacuum-compatible materials struck by the full-intensity electron beam will be damaged. Two experimental beam abort studies have been conducted on collimator test pieces in the present APS SR to inform the design of a fully-functional machine protection system for APS 4GSR operations at 200 mA. A comprehensive suite of diagnostics was utilized during the studies. The diagnostics used in these experiments are not new, but employed in different ways to obtain unique data sets. With these sets now in hand, we are developing new numerical tools to guide collimator design using PELEGANT [M. Borland, ELEGANT: A flexible SDDS-compliant code for accelerator simulation, Technical Report No. LS-287, Advanced Photon Source, 2000; Y. Wang and M. Borland, Implementation and performance of parallelized ELEGANT, in *Proceedings of the 2007 Particle Accelerator Conference*, http://cern.ch/AccelConf/p07/PAPERS/THPAN095.PDF, pp. 3444–3446], MARS [N. V. Mokhov and S. I. Striganov, Fermilab-conf-07/008-ad, *AIP Conf. Proc.* 896, 50 (2007)], and FLASH [B. Fryxell *et al.*, FLASH: An adaptive mesh hydrodynamics code for modeling astrophysical thermonuclear flashes, Astrophys. J. Suppl. Ser. **131**, 273 (2000); P. Tzeferacos *et al.*, Laboratory evidence of dynamo amplification of magnetic fields in a turbulent plasma, Nat. Commun. **9**, 591 (2018)].

DOI: 10.1103/PhysRevAccelBeams.25.043001

I. INTRODUCTION

The next decade of scientific research with hard x rays will be dominated by the development of diffraction-limited storage ring (SR) sources. The Advanced Photon Source Upgrade (APS-U) project [1] centers on the construction of a fourth-generation storage ring (4GSR) [2,3]. Specifically, the present double-bend achromat lattice will be replaced with a seven-bend system including reverse bending magnets yielding a horizontal emittance of 42 pm [4], a reduction of two orders of magnitude. The ultralow emittance, multibend achromat (MBA) lattice operating at 6 GeV and 200 mA comes with the concomitant challenge of handling electron beams of very high energy and power densities. In any storage ring, it is inevitable that the beam will be lost due to equipment failure, triggering of machine protection interlocks, or triggering of personnel protection interlocks. In the event of such beam aborts, the beam should ideally be absorbed in a well-shielded set of collimators (or beam dumps) that are capable of withstanding the energy and power densities. However, simulations with the particle-matter interaction program MARS [5] indicated many common ultrahigh-vacuum-compatible materials struck by the full intensity, primary APS-U beam will be damaged. The objective of the present work is to

*dooling@anl.gov

TABLE I. APS SR collimator experiments for APS-U.

Experiment No.	Study dates	Maximum beam current (mA)	Collimator material
1	May 18–19, 2019	67.4	Al-T6061, Ti6Al4V
2	Jan. 25–26, 2020	202.2	Al-T6061

conduct experimental studies which inform the design and construction of a robust, fully functional collimator system for 200 mA APS-U beam operations. Whole-beam dumps are fairly common in the present APS SR, on the order of 1–2 per week, and are likely to remain so in the SR upgrade.

Beam-irradiation damage from shock impacts has been observed at a number of accelerator facilities [6–9], and studies have been carried out most notably at CERN. Bertarelli provides a comprehensive review of analyses, simulations, and experiments [10]. Recent experimental and simulation efforts have been undertaken to couple energy-deposition and hydrodynamic codes [11–15]; however, these studies involved hadron particle beams. Except for damage to permanent magnets [16,17], concern in electron/positron SRs has focused on heating, pressure rise, and instabilities that come as a result of synchrotron photons, rather than hazards from the lepton beam itself [18].

In the APS SR, two whole-beam-loss studies have been performed thus far, the first in May 2019 and the second in January 2020; see Table I. An earlier experiment conducted in April 2012 examined the effects of whole-beam aborts on a tungsten (W) scraper used for diagnostics and provided evidence that significant damage can take place at dose levels of 2–3 MGy. Figure 1 illustrates the effects of individual beam aborts in the scraper's beam-facing surface.

The two most recent collimator experiments, conducted to create the conditions expected during APS-U SR beam dumps, are listed in Table I along with the maximum beam current, and collimator material tested. Because of its shorter radiation length, the titanium alloy showed significant melting during the first experiment [19] and was not tested during experiment 2.

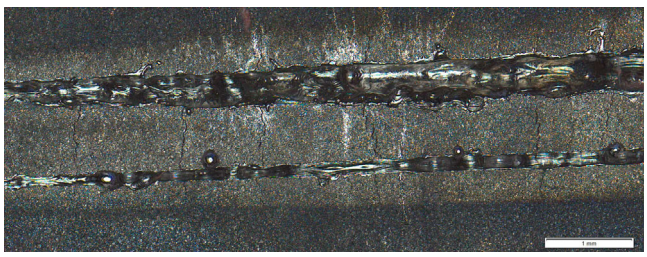

FIG. 1. Damage in the beam-facing surface of a W collimator after irradiation by separate beam aborts at 7-GeV, 100-mA stored current, yielding energy deposition of 2–3 MGy.

Diagnostics for these experiments included turn-by-turn (TBT) beam position monitors (BPMs), cameras, dc current transformers (DCCTs), and beam-loss monitors (BLMs). A different set of diagnostic techniques were used after the studies to examine the collimator test pieces including microscopy and metallurgy.

The manuscript is organized as follows. In Sec. II, we briefly discuss our plans to operate the APS-U SR using fast kickers for swap-out injection and why such a scheme cannot be used for whole-beam dumps. In Sec. III, we present several simulation results. Section III A describes modeling whole-beam aborts on collimators employing the static, particle-matter interaction code, MARS. In Sec. III B, thermal diffusion effects are considered as well as estimates of melting and vaporization. Section III C discusses preliminary efforts to couple beam dynamics, particle-matter interaction, and hydrodynamics codes to simulate the effects of high-energy-density (HED) beams on first-surface materials. High-energy densities are defined as energy densities exceeding roughly 10^{11} J/m^3 [20]; in aluminum this represents an acute dose of 37 MGy and in tungsten 5.2 MGy. Section IV describes the experiments conducted to irradiate collimator test pieces in the APS SR replicating conditions expected in the APS-U 4GSR. Results of the irradiation experiments related to beam-loss conditions are presented in Sec. V. Measurements made during the studies, specifically, beam spot size, emittance, implied dose, collimator emission, and beam-loss temporal behavior are given in Sec. V A. Post-irradiation measurements utilizing both destructive and nondestructive diagnostic methods are described in Sec. V B. Threshold behavior is observed between elastic, plastic, and hydrodynamic regimes as dose increases. These observations allow us to quantify damage in the test pieces and provide benchmark data for coupled simulations. In Sec. VI we estimate power densities likely present during the beam dump experiments and discuss why the absorbed power density (dose rate) as well as energy deposition (dose) are both important parameters to consider when designing a collimator system. Section VII summarizes the experimental work to date, and we discuss the path forward for the simulation effort. Section VIII provides concluding remarks.

II. OPERATIONAL CONSIDERATIONS

With on-axis swap-out injection [21,22], an entire bunch is kicked out of the SR and replaced with a new bunch. In the APS-U scheme [23], the swapped out bunch is directed to a dedicated beam dump (named the swap-out dump). Prior to bunch replacement, the targeted bucket receives a 150 μrad "decoherence" kick, which acts to increase the transverse spot size through decoherence over a period of approximately 250 turns (1 turn = 3.68 μs); at this point, a stronger kicker is triggered that directs the bunch into the

TABLE II. Basic timing-mode beam and machine parameters for the present APS SR and upgrade SR, including beam energy, E_b, beam current, I_b, total charge, Q_t, total electron number, N_q, stored energy, E_q, number of bunches, N_b, transverse emittances, ϵ_x and ϵ_y, and rms bunch duration, σ_t.

Machine	E_b (GeV)	I_b (mA)	Q_t (nC)	N_q	E_q (J)	N_b	ϵ_x (pm-rad)	ϵ_y (pm-rad)	σ_t (ps)
Present SR	7.0	100.0	368.0	2.3×10^{12}	2580.0	24	3110.0	40.5	41.0
Upgrade SR	6.0	200.0	737.0	4.6×10^{12}	4420.0	48	42.0	4.2	100.0

swap-out dump [24,25]. In this manner, the swap-out dump is protected. Interlocks prevent swap-out from occurring in the event that the target bunch is not kicked by the decoherence kicker.

In addition to the swap-out dump, APS-U will have a series of five whole-beam dumps that also function as horizontal collimators for Touschek-scattered particles. These devices are in high-dispersion locations in five consecutive sectors where the shielding wall is made from higher density material. Unfortunately, the approach of using decoherence to inflate the spot sizes of all bunches is not feasible for whole-beam aborts, since at 200 mA, the beam can arrive on the collimator in as few as 20 turns. A "fan-out" kicker scheme would allow the bunches to be spread vertically on the collimators, which would reduce the degree of damage. Beam dynamics simulations indicate a fan-out kicker system can protect the collimators. Such a kicker is planned for APS-U and will be triggered whenever a beam abort is detected. However, there is no possibility to delay the beam abort should the fan-out kicker fail to fire, so in this case the collimators would be unprotected.

Basic timing-mode beam parameters for the present APS SR and SR upgrade are given in Table II. The machine circumference is 1104 m in both present and upgrade designs. Though the electron energy drops from 7 to 6 GeV in the new machine, the circulation period, T_o remains essentially the same at 3.68 μs with a harmonic number of 1296 (rf frequency = 351.9 MHz). In uniform fill patterns, bunch spacing is T_o/N_b where N_b is the number of bunches. The number of bunches listed in Table II represent "timing mode" fill patterns; other patterns are available, most notably "brightness mode" where $N_b = 324$.

III. SIMULATIONS AND DAMAGE ESTIMATES

The purpose of the simulation effort is to develop numerical tools that can be used to understand possible damage to collimators and ideally guide construction of robust collimator designs and machine protection systems for HED electron beams in 4GSR light sources generally, and specifically for APS-U.

A. Static collimator dose simulations

Simulations of a beam-dump collimator dose have been carried out with MARS employing electron loss distributions generated by PELEGANT [26,27]. PELEGANT is a parallel particle tracking code that includes the ability to simultaneously model single- and multibunch collective effects; other relevant features include modeling rf trips, time-dependent kickers, and collimators of various types.

Modeling of the beam aborts included both collective effects and nonlinear dynamics. For collective effects, the short-range longitudinal and transverse impedances were included [28]. Since the beam abort is performed by removing or muting the drive signal to the rf amplifiers, the ring-down of the rf cavities was included using the estimated average parameters of the sixteen installed rf cavities ($R_a = 11.2\ M\Omega$, $Q_0 = 49 \times 10^4$, $\beta = 2.20$). The RFMODE element in PELEGANT supports realistic cavity modeling with feedback [29] (to properly model bunch-train transients) and also allows muting the rf drive signal at a defined point. For linear and nonlinear dynamics, we used element-by-element tracking with a calibrated lattice model based on measurements taken before the beam abort study. The lattice model included the vertical beam bumps used to vary the location of the beam strike on the collimator.

A total of 20 beam aborts were performed during the second experimental study, with various fill patterns and total beam current. To further improve the correspondence between simulation conditions and reality, the waveforms from the bunch current monitor were used to create the bunch patterns for the simulations. PELEGANT requires that all simulation particles represent the same charge, so variation in charge per bunch was modeled by varying the number of particles in the bunches. To limit the running time of the simulations, the total number of simulation particles in all bunches was limited to 1 million.

Prior to the beam abort studies, initial MARS simulations of APS-U conditions indicated that even a single 6-GeV bunch from a 48-bunch fill pattern at 200 mA (15.3 nC/bunch) could damage most commonly used accelerator materials including aluminum, titanium, copper, and tungsten.

We examined the effect of whole-beam dumps employing the MARS collimator geometry of Fig. 2. The horizontal collimator is modeled with a radius of curvature of 0.865 m. Figure 3 compares beam strikes on aluminum and tungsten collimators in terms of electron-positron flux, ϕ_{ep}. In both cases, the same input loss distribution is employed. In these early simulations, the lost electron distribution strikes with a depth of 0.6 mm at the collimator apex. No significance is attached to this depth other than the requirement to fully

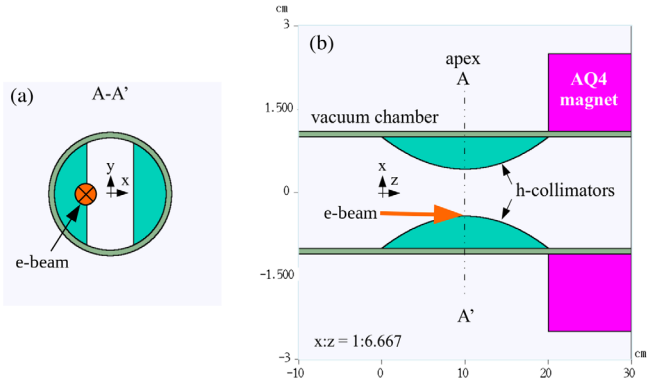

FIG. 2. Simplified horizontal collimator geometry implemented with MARS. Shown in (a) is a cross section through the collimator apex at $z = 10$ cm with the e-beam into the page, and in (b) is an anamorphic view of a lateral slice at beam elevation ($y = 0$).

strike the collimator for comparison of dose and temperature transients in different materials. The apex is the location of the collimator closest to the beam centerline and is modeled here to occur at $x = -0.42$ cm, $z = 10$ cm. The horizontal collimator is modeled as a symmetric structure also used to stop Touschek and injection losses with an outboard apex at $x = +0.42$ cm. The actual collimator test pieces are only 4-cm long in the z direction but maintain a similar radius of curvature on the beam-facing surface as presented in Figs 2 and 3; see Sec. IV. As will be shown in Sec. V, a length of 4 cm is sufficient to view the full extent of the beam-collimator interaction region.

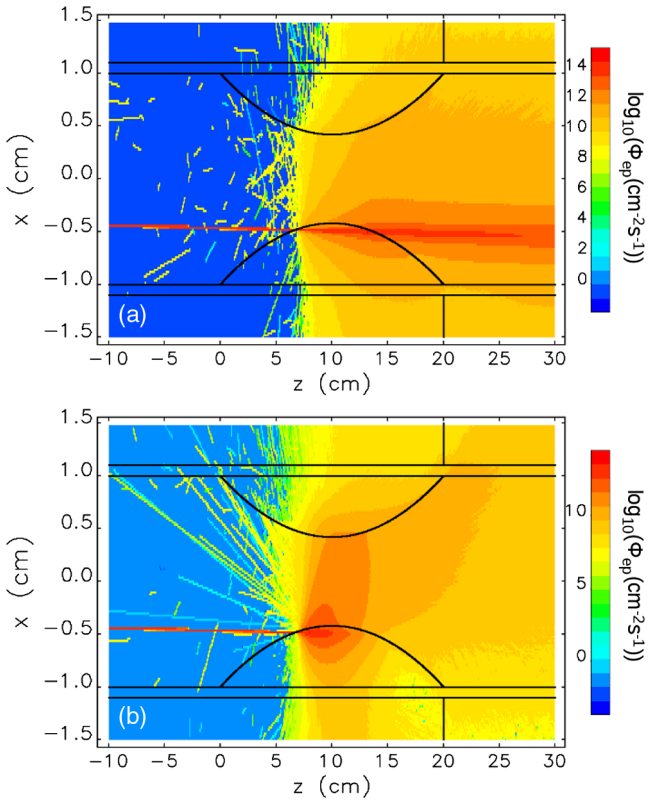

FIG. 3. Static MARS simulation of combined electron-positron flux in collimators fabricated from (a) aluminum and (b) tungsten. The x-y-z voxel dimensions are $0.02\ \text{cm} \times 0.1\ \text{cm} \times 0.1\ \text{cm}$ centered at beam elevation ($y = 0$).

In the case of aluminum, the physical radiation length is $t_R = X_o/\rho = 8.9$ cm, where the geometric radiation length $X_o = 24.01\ \text{g/cm}^2$ [30] and the density $\rho = 2.70\ \text{g/cm}^3$. A portion of the beam is scattered, but most of the energy passes through the collimator [31]. On the other hand, for the tungsten collimator with $t_R = 0.35$ cm [32], the primary beam is almost completely attenuated and only secondary radiation remains.

However when acute dose levels exceed 2 MGy, static solutions are not always accurate. Heated material in the beam-strike region can be deformed, melted or expelled, especially in the case of high-Z, high-density (short radiation length) metals such as tungsten, as shown in Fig. 1. As the collimator is eroded, its effectiveness for shielding downstream components is reduced. Eventually, this may allow a beam strike on a vacuum chamber, with potential vacuum-integrity consequences.

The temperature rise in an irradiated material volume between initial temperature T_1 and final temperature T_2 can be approximated by

$$q_V(x) = \int_{T_1}^{T_2} \rho(x,T) c_p(T) dT(x), \tag{1}$$

where q_V is the energy deposited per unit volume, ρ is the material density (a function of position and temperature), and c_p is the specific heat at constant pressure. Assuming a constant density and average specific heat over the temperature range, the final temperature may be expressed as

$$T_2 \approx \frac{q_V(x)}{\rho(x)\bar{c}_p} + T_1 = \frac{DA_w}{C_m} + T_1, \tag{2}$$

where D is the dose, A_W is the atomic weight, and C_m is the molar specific heat. Prior to the solid-to-liquid phase change, the specific heat of aluminum increases with temperature [33]; whereas, the density decreases only slightly. Equation (2) thus yields a conservative result overestimating the temperature rise. Equations (1) and (2) also assume no phase change in the material nor diffusion due to temperature gradients. For most metals, C_m is approximately 25 J/mole-K.

Employing Eq. (2), final peak temperatures T_2 in Al, Ti, Cu, and W are presented in Table III based on the dose from one bunch of a 48-bunch fill pattern at 6 GeV and 200-mA (15.3 nC/bunch) for APS-U beam parameters assuming $T_1 = 300$ K. The data in Table III suggest these elements commonly found in beam-facing accelerator components will be damaged by a single bunch of an APS-U beam in timing mode.

TABLE III. Examples of final peak temperatures in Al, Ti, Cu, and W using Eq. (2) based on the dose from a single 15.3-nC bunch at 6 GeV with APS-U beam parameters ($T_1 = 300$ K). T_m and T_v represent the melting and vaporization temperatures.

Material	$D_{\max}$ (MGy)	A_w (g/mole)	C_m (J/kg-mole)	T_2 (K)	T_m (K)	T_v (K)
Al	1.96	26.98	24.20	2285	856	2743
Ti	3.03	47.87	25.06	5830	1941	3560
Cu	2.94	63.55	24.44	7650	1358	2835
W	2.53	183.84	24.27	19,300	3695	6203

In the present APS storage ring, again using Eq. (2), the final peak temperatures in Al and W due to the instantaneous dose from a 100-mA, 7-GeV whole-beam dump are 842 and 22,150 K, respectively. MARS calculates T_2 accounting for the variation of c_p with temperature [33] as long as added heat does not exceed that necessary to cause a phase transition. In the case of aluminum for a whole-beam dump in the present APS SR, the maximum temperature predicted by MARS is 768 K [34], less than the melting point. Unfortunately, a similar calculation for tungsten will be inaccurate since the deposited energy is sufficient to both melt and vaporize the metal. Thus, based on the peak dose and material properties, the damage observed in the tungsten collimator shown in Fig. 1 should be expected. Further at 100 mA in the present machine, damage to aluminum is not expected, which is consistent with APS experience.

B. Estimation of thermal diffusion effects

The beam typically takes three to five turns (~11–18 μs) to be completely lost, allowing thermal diffusion to diminish the degree of material damage by reducing the temperature rise. Measured time profiles of beam losses are presented in Sec. V A. Thermal diffusion can be approximately included by convolving the dose map with a Gaussian spread function [35] with $\sigma_d = \sqrt{\alpha \Delta t}$, where α is the thermal diffusivity and Δt is the time over which energy is deposited. Using this, an improved method was developed for estimating material melting and vaporization.

The method begins by creating a two-dimensional dose map D_{ij} using the lost-particle coordinates from a beam abort simulation (it is assumed that all voxels with the same x and y coordinates receive the same dose). More specifically, $D_{ij} = (Q_{ij} d)/(\Delta x \Delta y)$, where Q_{ij} is the charge impacting the pixel of size Δx by Δy, and d is the dose per unit charge, computed from the collisional stopping-power data from the NIST ESTAR database [36]. Since σ_d sets a scale for how rapidly the thermally diffused distribution can vary, the transverse size of the voxels for D_{ij} was chosen to be $\Delta x = \Delta y = \sigma_d/6$. The Gaussian parameter for the thermal diffusion spread function was taken to be $\sigma_d = \sqrt{\alpha \Delta t_{90}}$, where $\Delta t_{90} = t_{95} - t_5$, where t_{95} (t_5) is the time, according to the simulation, at which 95% (5%) of the beam has been lost. Convolving D_{ij} with the thermal-diffusion Gaussian provides an effective dose map, $\hat{D}_{ij}$.

The effective dose map can be used to estimate the volume of material that is melted or vaporized. Assuming constant specific heat capacity C_p for the solid phase, melting is indicated if

$$\hat{D}_{ij} > (T_m - T_1) C_p + \Delta H_m, \tag{3}$$

where ΔH_m is the enthalpy of melting and T_m is the melting temperature. Vaporization is indicated if

$$\hat{D}_{ij} > (T_m - T_1) C_p + \Delta H_m + (T_v - T_m) C_l + \Delta H_v, \tag{4}$$

where C_l is specific heat capacity (assumed constant) of the liquid phase, ΔH_v is the enthalpy of vaporization, and T_v is the temperature of vaporization. The volume of melted or vaporized material is estimated as the number of melted or vaporized pixels times the volume behind each pixel, the latter being $\Delta x \Delta y \Delta z_{ij}$, where Δx and Δy are the pixel sizes and Δz_{ij} is the depth of material in the beam direction, which varies with transverse coordinates.

This method was applied to the conditions of the second collimator experiment, using data from simulations of the beam aborts performed with PELEGANT [26,27]. While it is difficult to compare these predictions quantitatively to experiments, the simulations provide other predictions that can be directly compared to measurements. Here, we outline the simulation methods and predictions of melting and vaporization.

The machine lattice was measured prior to the experiment using the linear-optics-from-closed-orbit method [37] to an accuracy of about 1% in beta functions and dispersion. Although the bunches were started with close-to-equilibrium properties, the simulations were run for 10,000 turns (about 2.4 damping times) to ensure equilibration. Averaging over the last 2,000 turns provides predictions of the equilibrium properties, as shown in Fig. 4. Cases where the predicted vertical emittances are smaller do not agree well with measured vertical emittance values. This is due to an apparent error in the lattice setup that was not recognized until after the studies took place. The variation in the vertical emittance resulted from inclusion of sextupole magnets inside the vertical bump that was used to move the strike location on the target. This error shows significant (~10%) lattice function beats in the calibrated model, but it is unclear if the lattice as set up for the experiments had these beats. However, this detail is thought to be of minor consequence given the effect of thermal diffusion, as shown below.

Figure 5 shows the peak dose in aluminum as a function of current based on these simulations. Results including thermal diffusion are shown along with the raw dose calculated using the collisional stopping power, S_{pc} [36]

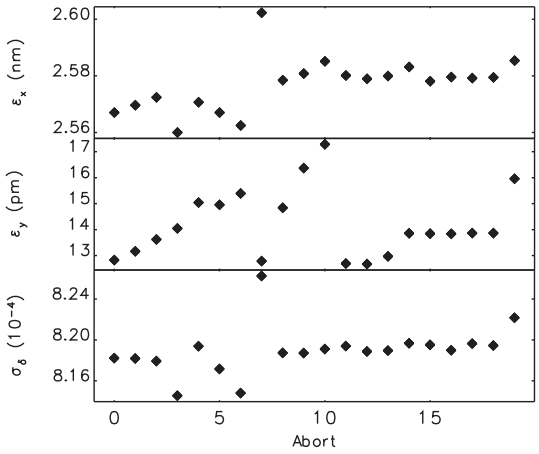

FIG. 4. Simulated equilibrium beam parameters for the second collimator experiment, from particle tracking simulations with PELEGANT. The horizontal axis label, "Abort" refers to the sequence number of the beam dumps (see Table VI).

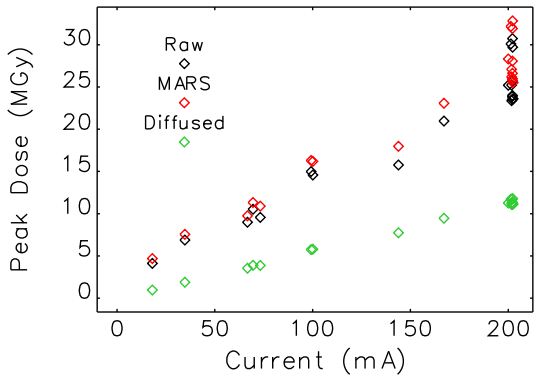

FIG. 5. Simulated peak dose in aluminum for the second collimator experiment. Shown are the raw results, MARS results, and those including thermal diffusion.

at 6 GeV and MARS simulations. MARS peak dose levels exceed the raw values by roughly 9%, likely due to MARS including the developing shower contribution. The effect of thermal diffusion is to decrease the peak dose by about a factor of 2.5. The predicted raw peak dose at 200 mA varies among the different cases due to variation in the transverse beam dimensions. The effect of this variation is eliminated in the diffused dose map. The peak dose with thermal diffusion is linear in the total current, as might be intuitively expected. Figure 6 shows the predicted vertical extent of liquefied aluminum based on the thermally diffused dose maps. (Note that no vaporization of aluminum is predicted.) The predicted curve saturates as the current increases, which can be understood by recalling that the occurrence of liquefaction is subject to a threshold. As the current increases, more of the impacted volume of the collimator is pushed over the threshold. However, the volume cannot increase without limit as the footprint of the beam on the collimator is limited.

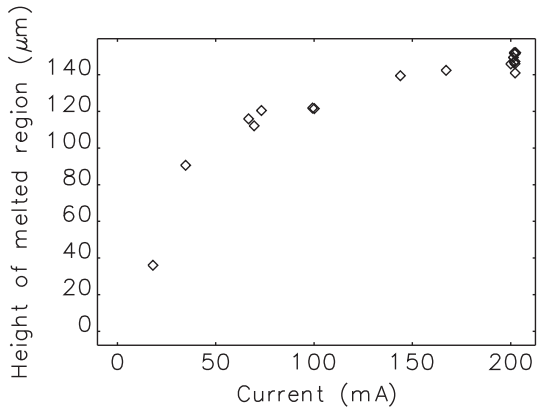

FIG. 6. Vertical extent of the liquified-aluminum region for the second collimator experiment, based on the thermally diffused simulated dose map.

These predictions are somewhat difficult to correlate with the experimental results. It is not clear from this simple analysis whether melted material resolidifies, flows, or explodes from the surface. However, there are some aspects of the simulations that can be compared to the experiments, as described below. In addition, these simulations are a step toward more comprehensive simulations that will enable more detailed comparisons to experiments.

C. Initial hydrodynamic simulations of the collimator

Simulations of dynamics involve coupling a static particle-matter interaction program with a hydrodynamics code. Future work will involve the inclusion of beam dynamics modeling to track shower components downstream of the collimators. Here we highlight initial steps in that direction.

Early coupling work was carried out by Wilson [38] and Mokhov [6] for 20-TeV proton beams in the Superconducting Super Collider. More recent coupled simulation work focused on beam loss in the Large Hadron Collider [11,12] and the proposed Future Circular Collider [14,15]; again effort was devoted exclusively to hadron (proton) rather that lepton beams. Modeling employed FLUKA [39] for particle-matter physics along with LS-DYNA [40] or AUTODYN [41] for hydrodynamics. Coupled simulations reported in these references focused on cylindrically symmetric (2D) geometry. Full 3D, coupled simulations were carried out for LHC collimators as well [13].

A range of time intervals is important in the simulations: (1) deposition time or intrabunch time, (2) interbunch time dependent on the fill pattern, and (3) turn period, $T_o = C/c = 3.68$ μs, where the circumference of the SR, $C = 1104$ m and c is the speed of light. Loss monitors and BPMs indicate that the loss period varies, but has not been observed to be less than two turns, full width half maximum (FWHM). We chose a 48-bunch fill pattern to do initial

simulations with FLASH [42,43]. FLASH is a hydrodynamics plasma code which includes magnetohydrodynamic (MHD) effects; here the MHD component is turned off with only the hydrodynamics solver invoked. In the case of a 48-bunch fill pattern, the interbunch spacing, $\Delta t_b = T_o/N_b = 77$ ns, where N_b is the number of bunches. The damage observed in the collimators suggested a 2D approach was a reasonable starting point. In this case, Cartesian coordinates (x,y) were chosen, where x represents the horizontal dimension measured with respect to the nominal beam centerline, and y is the vertical dimension measured relative to beam elevation. MARS transverse dose maps were provided to FLASH with 20 μm by 20 μm resolution. The FLASH simulation domain (0.2 mm × 0.2 mm) and MARS dose map overlaying this domain are presented in Fig. 7. The peak dose for this case of a single 15.3-nC bunch (9.58×10^{10} electrons) is 2.0 MGy. The dose map is scaled from a simulated APS-U 48-bunch, 200-mA whole-beam dump at 6 GeV. Helium is needed in the vacuum region as a low-density material to satisfy needs of the hydrodynamic solver; the presence of He contributes negligibly to the simulation results [44].

FLASH typically deals with fluids in the form of plasmas, employing equations of state to determine local pressure, density, and temperature conditions, however the material in the collimator starts in solid form. To handle the phase transition from solid to fluid, a release criterion based on the dose is established. The release condition may be written in a form similar to Eq. (4),

$$D_{i,j} > C_p(T_m - T_r) + \Delta H_m + f_l C_l(T_v - T_m) + f_{vap}\Delta H_v, \tag{5}$$

where f_l and f_{vap} are fractions of the liquid and vapor phase energies with values between 0 and 1. In the first phase of simulations, $f_l = f_{vap} = 0$ was chosen; meaning the collimator material was released to fluid form after the melt condition was satisfied. Figure 8 shows the effects of dose deposited by a 200-mA, 48-bunch beam over five turns (18.4 μs) at one-fifth of the intensity of a single turn.

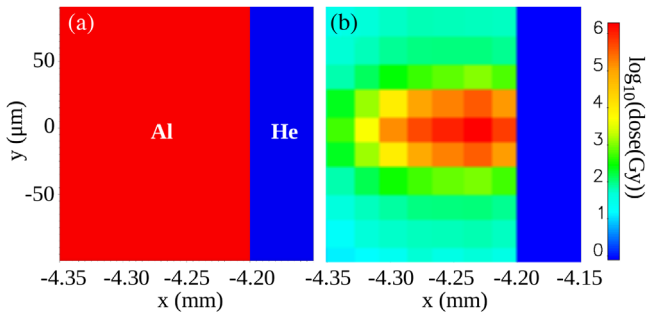

FIG. 7. (a) FLASH 2D simulation domain (initial condition) and (b) the MARS dose map overlaid on the same region.

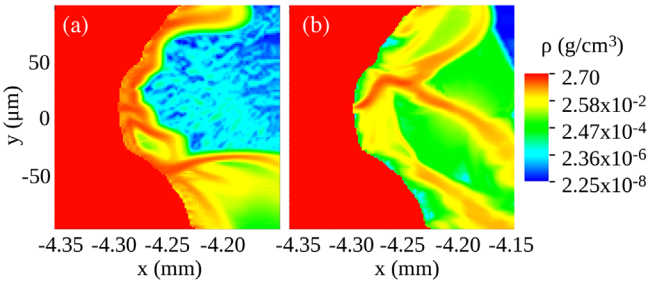

FIG. 8. FLASH 2D-density simulation of a 48-bunch, 200-mA beam dump in aluminum spread over five turns. The domain is the same shown in Fig. 7. The results are shown at (a) 1.28 μs [0.35 turn] and (b) 4.37 μs [1.19 turns].

Note the rapid change in conditions from solid to high- and low-density fluid. In this simulation, horizontal motion of the beam due to energy loss and dispersion has been ignored. The simulation indicates regions of relatively high-density fluid (vapor or plasma) forms within and outside the trench cleared by the beam. This fluid will interact with and scatter the beam that has not yet struck the surface. The scattering effect may play a role in limiting damage to the material remaining in the collimator below the beam. Scattering caused by interaction with a high-density vapor generated from a beam dump on a cryogenic-cooled, solid xenon target has been investigated numerically with PELEGANT and showed promising results [45].

By the time of the second frame shown in Fig. 8(b), ablation of the surface has largely stopped. Compared with the microscopy data, the simulation using the melt condition for release is too aggressive. Work is presently under way to refine the model in FLASH. For example, guided by the discussion in Ref. [46] we are setting the release condition to higher temperatures to satisfy vaporization conditions. The rapid release and conversion of solid voxels to fluid however can cause numerical issues which we are presently addressing.

Reducing the MARS domain to 0.3 mm × 0.3 mm and overlaying a 128 × 128 transverse grid yields voxels of 2.34 μm on a side; significantly smaller than the beam spot sizes. The dose distribution at the apex for an APS-U 200-mA, 48-bunch fill pattern is shown in Fig. 9; x- and y-dose profiles through the data of greatest integrated dose are presented in the left and right insets. (Also, the contour plot has been rotated by 90°, now showing the x direction along the vertical axis.) The dose map presented in Fig. 9 is scaled to that of a single bunch. Using the same PELEGANT input loss distribution, peak dose is found to be 3.1 MGy; this grid is being used for on-going studies with FLASH.

After the January 2020 experiment, the PELEGANT simulations discussed above were carried out and new loss distributions were produced. The MARS-generated, whole-beam dump dose map for one of the 200-mA cases is presented Fig. 10; specifically, this is the eighth shot (SN08) carried out in the sequence of 20 loss events and the

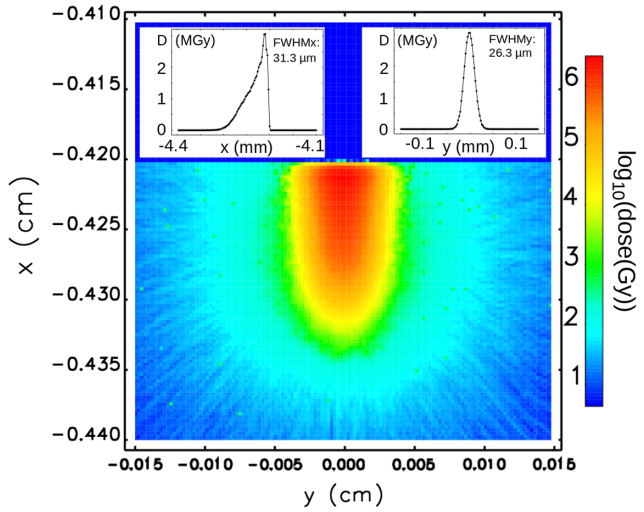

FIG. 9. Dose map at the collimator apex for a simulated APS-U 48-bunch, 200-mA whole-beam dump fill pattern using a 128×128 grid over an x-y domain of 0.3 mm by 0.3 mm (voxel size: 2.34 μm). The dose is scaled to that for a single bunch. The insets plot the x- and y-dose profiles at the location of maximum integrated dose, yielding $\mathrm{FWHM}_x = 31.3$ μm and $\mathrm{FWHM}_y = 26.3$ μm.

first of the 200-mA cases. Experimental data for SN08 and other beam dumps are presented in the following sections. The increased size of the distribution relative to that for the APS-U case is evident.

In the simulation results presented here, the dose map is static; in reality, the beam moves inboard after the beam dump is initiated due to synchrotron radiation and other loss mechanisms. We are presently working on coupling the density modifications from FLASH back into MARS. In Sec. VI we discuss in greater detail how loss intensity is affected by temporal and spatial distribution based on experimental results.

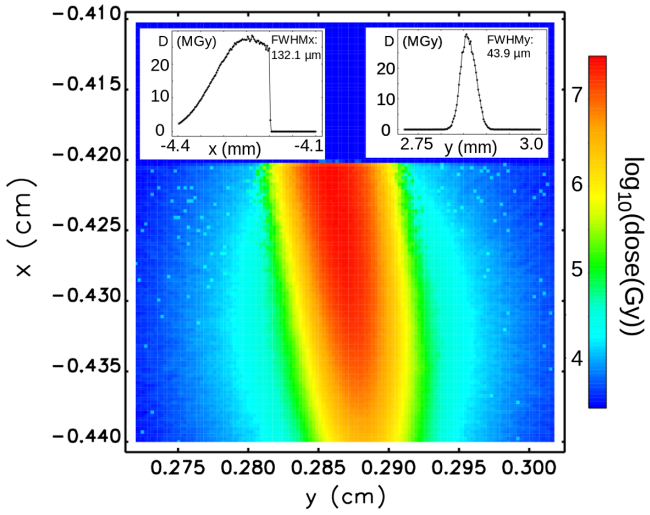

FIG. 10. Dose map at the collimator apex for a 200-mA, whole-beam dump from the January 2020 experiment simulating the eighth loss event (SN08). Note the increased size of the footprint relative to the APS-U case presented in Fig. 9. The x- and y-dose profiles plotted at the location of maximum integrated dose yield $\mathrm{FWHM}_x = 132.1$ μm and $\mathrm{FWHM}_y = 43.9$ μm.

IV. EXPERIMENTAL METHODS

To test the effects of APS-U HED electron beams on accelerator technical surfaces, we utilized the APS SR to provide approximately equivalent conditions. The beam was dumped by muting the rf drive signal to the SR rf amplifiers. A variable-position, horizontal collimator mounted to a scraper assembly was used to provide a means of positioning a target close to the beam path. The assembly was located in the sector 37 (S37) long rf straight section. A plan view of the assembly is presented in Fig. 11. This location is 2 m downstream of the fourth rf cavity in S37. [In the APS SR, sectors 36 through 40 are devoted to rf cavities and injection; sectors 1–35 are the domain of user activities and include small-gap undulator insertion device (ID) vacuum chambers.]

A. Collimator surface

The experiments made use of an existing, unused horizontal beam scraper assembly. Two collimator test pieces were mounted on the end of the scraper jaw, as shown in Fig. 11. An oblique drawing of the collimator test piece as well as an actual manufactured item are presented

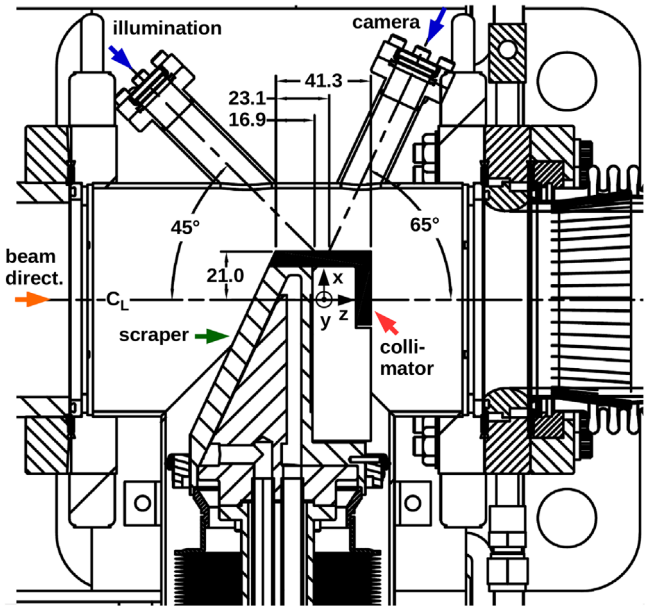

FIG. 11. Horizontal collimator assembly plan view. The collimator test pieces are stacked in the y direction so that only one is visible in this view; in addition, the collimator pieces are shown fully inserted, past the centerline. In the experiments, the collimators are withdrawn to a parking position allowing the beam to circulate. Dimensions are given in mm.

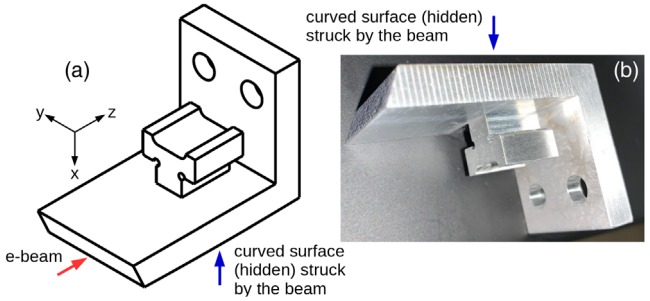

FIG. 12. Collimator test piece. (a) Oblique view. (b) The manufactured article showing 1-mm-spaced rulings along one of the lateral surfaces. Distance along the chord on the beam-facing surface is 41.5 mm.

in Fig. 12. The beam-facing surface is hidden, below the image. The surface facing the beam is machined to have large radius (0.8 m) creating an apex near the center of the collimator. The apex is the location on the collimator we expect the beam to strike first as it loses energy after rf muting. The machined radius yields an apex approximately 0.3 mm above the chord connecting the upstream and downstream ends of the collimator piece. Note that Figs. 2(b) and 3 show anamorphic, idealized views of the geometry in the x-z plane ($y = 0$) used in MARS. The actual collimator test pieces presented in Figs. 11 and 12 are not as long in the beam (z) direction as shown in the MARS geometry, but the curvature of the exposed surface is still present.

Prior to assembly, a microscope system was used to obtain a view of the machined radius as well as surface roughness. An anamorphic image of the collimator surface taken with a Keyence VR3200 microscope is shown in Fig. 13. The view is magnified in the vertical (x) direction 3000 times. The measurement was made on the aluminum test piece installed for the May 2019 experiment; the surface roughness was found to be 2.7 μm. The aluminum test pieces used in the January 2020 study had a significantly reduced surface roughness value of 0.45 μm. We note in the latter experiment only aluminum test pieces were irradiated.

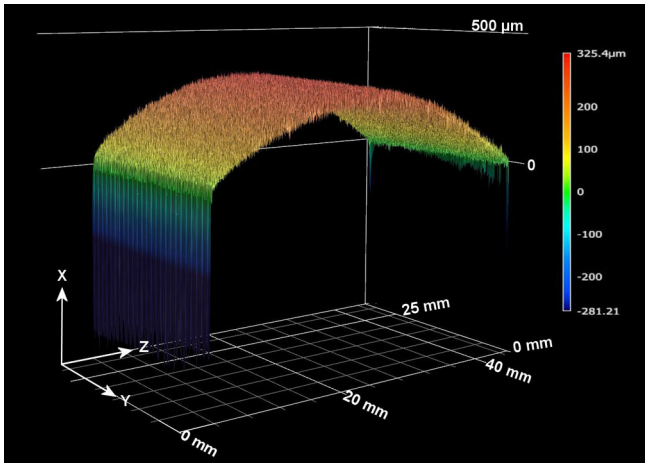

FIG. 13. An anamorphic view of the collimator surface showing curvature and roughness for the aluminum test piece used in May 2019.

TABLE IV. Lattice parameters at the collimator location in sector 37. Beam sizes are determined using $\epsilon_x = 2.58$ nm, $\epsilon_y = 15$ pm, and $\sigma_{\Delta p/p} = 8.2 \times 10^{-4}$.

Parameter	Symbol	Design value	Units
Horizontal beta function	β_x	4.0	m
Vertical beta function	β_y	6.0	m
Horizontal dispersion function	η_x	0.059	m
$\frac{d\eta_x}{ds}$	η_x'	0	⋯
Vertical dispersion function	η_y	0	m
$\frac{d\eta_y}{ds}$	η_y'	0	⋯
Horizontal beam size, rms	σ_x	111	μm
Vertical beta size, rms	σ_x	9.5	μm

Optical and mechanical monitoring of the collimator surface was performed during the experiments. The collimator surface was imaged using a diagnostic camera. Details of the camera apparatus are outlined in Ref. [47]. The horizontal (x) position of the collimator surface was monitored using a linear variable differential transformer (LVDT). LVDT calibration is also discussed in Ref. [47].

B. Lattice parameters at the collimators

Since the electron beam emittance is ~2.5 nm in the APS SR, we employ an insertion with modified lattice parameters at the location of the collimators in order to maximize energy deposition. Lattice parameters at the scraper location in S37 are summarized in Table IV. Beam size estimates are made using averaged PELEGANT simulation results for emittances

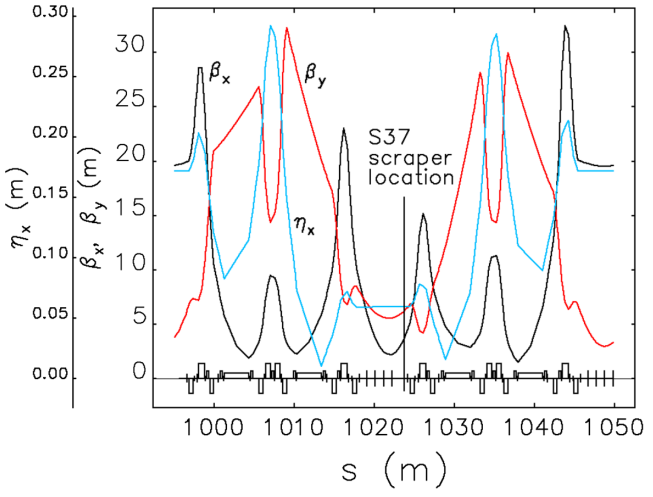

FIG. 14. The reduced-horizontal-beam-size lattice functions in S37 and S38. The collimators were positioned at $s = 1023.78$ m. Horizontal and vertical tunes were 36.169 and 19.241.

and energy spread from Sec. III B with $\epsilon_x = 2.58$ nm, $\epsilon_y = 15$ pm, and $\sigma_{\Delta p/p} = 8.2 \times 10^{-4}$.

A triple reduced-horizontal-beam-size (RHB) lattice was developed to minimize the spot size at the S37 scraper location. The lattice was modeled with PELEGANT. Twiss parameters for the RHB lattice in S37 and S38 are plotted in Fig. 14; the collimator/scraper assembly was located at $s = 1023.78$ m.

V. RESULTS

In addition to the beam-related measurements mentioned in this section, temperature and rf cavity chamber pressure were also monitored; these results are found in Ref. [47].

A. Observations during irradiation studies

Beam dumps were monitored by both turn-by-turn (TBT) beam position monitors (BPMs) and fast beam-loss monitors (BLMs). Both diagnostics provide temporal information on the beam losses.

1. Electron beam emittance, current, and current density

The electron beam size was measured during the experiments using a hard x-ray pinhole camera at S35. Using the beam sizes and the design lattice functions at the pinhole location allows us to infer the emittances. The beam size and current density at the scraper location are then calculated using the beam emittances and lattice functions.

By way of example, horizontal and vertical emittances just prior to a 200-mA beam dump are plotted in Fig. 15 along with scraper position and current for the case of $y_{\text{bump}} = 2.6$ mm. The plot ends with the beam dump. As shown in Fig. 15, variations in vertical emittance with current were observed prior to beam dumps, whereas horizontal emittance essentially showed no change. The stored beam

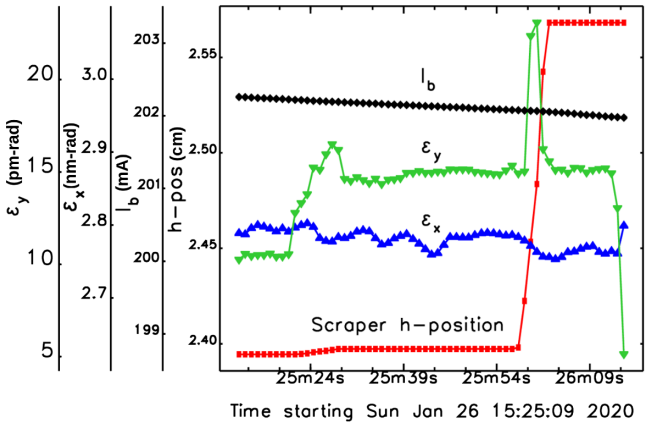

FIG. 15. Beam emittances, scraper position, and beam current for a 200-mA beam with a 2.6 mm vertical bump. The plot ends with the beam dump.

current was measured using a DCCT. The slope of current versus time becomes more negative as the scraper was inserted to its final position indicating a reduction in lifetime.

A position of 2.57 cm corresponds to the collimator apex at $x = -2.0$ mm relative to the beam centerline. After the collimator reached this position, the beam abort was initiated. The beam dump cases were separated by vertical (y) orbit bumps with a nominal spacing of 0.4 mm. The electron beam position was located vertically with respect to the collimator through observations of beam lifetime variation with vertical position. Near the gap between the upper and lower collimator test pieces, beam lifetime was observed to increase. Details of this process are outlined in Ref. [47].

Table V lists the beam aborts in sequential order for the highest beam currents (> 15 mA) during the first experiment where both Al and Ti alloys were tested. Beam dumps below 15 mA displayed no damage. Also presented in the table are vertical beam offset, current, emittances, rms spot sizes, estimated peak dose based on Gaussian transverse profiles [see Eq. (8)], and the maximum dose from MARS simulations. In Table V, the MARS results employ the APS-U loss distribution scaled by beam current,

$$D_U = D_{Ut} I_b / 200, \tag{6}$$

where $D_{Ut} = 3.1$ MGy/bunch (48 bunches) = 149 MGy and I_b is the beam current in mA. PELEGANT loss distributions were not generated for the May 2019 experiment. Table VI presents the same data for the second experiment where only Al-alloy test pieces were irradiated. In addition, PELEGANT loss distributions for each of the 20 beam dumps were employed to generate the raw dose maximums, D_{raw} presented in Fig. 5 using the collisional stopping power S_{pc} at 6 GeV. The loss distributions were also used as MARS input to determine peak dose, D_{ex}. Assuming Gaussian distributions, the peak current density j_b is calculated as

$$j_b = \frac{I_b}{2\pi\sigma_x\sigma_y}. \tag{7}$$

At 200 mA, calculated current densities reach 39 A mm^{-2}, approximately 5 times the damage threshold observed in aluminum. Initial dose for a normal-incident, Gaussian-distributed, monoenergetic beam may be expressed in a form similar to Eq. (7) as

$$D_G = S_{pc} \frac{N_q}{2\pi\sigma_x\sigma_y}, \tag{8}$$

where N_q is the total number of circulating electrons. At 6 GeV, $S_{pc} = 2.02$ MeV cm^2 g^{-1} in titanium and 2.153 MeV cm^2 g^{-1} in aluminum. The radiative stopping power S_{pr} (246.7 MeV cm^2 g^{-1} for Al and 373.7 MeV cm^2 g^{-1} for Ti) is much larger than S_{pc}.

TABLE V. Material and chronological sequence number (SN), number of bunches N_b, y offset, beam current, I_b, charge per bunch, Q_b, emittances, spot sizes $\sigma_{x,y}$, current density j_e, peak Gaussian profile dose D_G, and maximum dose predicted by MARS using the APS-U loss distribution, D_U, during the May 2019 S37 collimator study. Mat'l Al refers to aluminum alloy T6061 and Ti stands for titanium alloy Ti6Al4V.

Mat'l/SN	N_b	y_{off} (mm)	I_b (mA)	Q_b (nC)	ϵ_x (nm)	ϵ_y (pm)	σ_x (mm)	σ_y (μm)	j_e (A/mm^2)	D_G (MGy)	D_U (MGy)
Al/04	27	3.8	17.1	2.33	1.87	8.2	0.1047	7.0	3.71	2.94	12.7
Al/05	54	4.3	33.1	2.26	1.84	10.1	0.1042	7.8	6.48	5.13	24.6
Al/06	108	4.8	67.4	2.30	1.89	14.7	0.1052	9.4	10.85	8.60	50.2
Ti/11	27	−3.3	15.9	2.17	1.87	4.54	0.1048	5.2	4.64	3.45	11.8
Ti/12	54	−3.8	32.1	2.19	1.85	4.98	0.1044	5.5	8.90	6.62	23.9
Ti/13	108	−0.7	66.9	2.28	1.84	24.3	0.1042	12.1	8.45	6.28	49.8
Al/14	108	1.2	64.1	2.18	1.79	9.58	0.1032	7.6	13.00	10.31	47.7

The radiative component should not appreciably contribute to local heating in the case of aluminum ($(X_o/\rho)_{Al} = 8.9$ cm); however, this is probably not true for the titanium alloy ($(X_o/\rho)_{Ti} = 3.56$ cm).

The ratio $D_U/D_{ex} = 5.02 \pm 0.81$ for all entries in Table VI and 5.36 ± 0.50 for the eleven 200-mA cases. These values are roughly consistent with the ratio of the footprint areas given by the product of the FWHM beam sizes presented in Figs. 9 and 10: $(132.1/31.3)(43.9/31.3) = 5.92$. Nearby S38A:P2 TBT BPM centroid measurements at 200-mA indicate the beam moving inboard at a rate of -132 μm per turn; here horizontal dispersion η_x is 78 mm; however, as shown in Table IV, at the collimator position $\eta_x = 59$ mm. The rate of inboard motion at the collimators is then approximately -100 μm/turn. PELEGANT simulations for APS-U predict -80-μm/turn horizontal motion for a whole-beam dump at 200 mA. In the simulations, an electron is considered lost when its horizontal position places it anywhere within the collimator.

Equation (8) describes the beam as if it were normally incident on the collimator. Instead prior to phase changes, the electrons are sheared off horizontally at the collimator apex; as discussed below, this process happens over 3–5 turns depending on current. One would then expect the collimator apex to be irradiated by several regions of the beam cross section over the period of the dump and thus experience a higher dose than that given by Eq. (8). In other

TABLE VI. Chronological sequence number (SN), number of bunches N_b, y offset, beam current, I_b, charge per bunch, Q_b, emittance, spot sizes $\sigma_{x,y}$, current density j_e, peak Gaussian profile dose D_G, peak raw dose D_{raw}, maximum dose levels simulated with MARS from the January 2020 experiment, D_{ex} and dose scaled to APS-U conditions, D_U. The target material in both test pieces is Al-T6061.

SN	N_b	y_{off} (mm)	I_b (mA)	Q_b (nC)	ϵ_x (nm)	ϵ_y (pm)	σ_x (mm)	σ_y (μm)	j_e (A/mm^2)	D_G (MGy)	D_{raw} (MGy)	D_{ex} (MGy)	D_U (MGy)
00	27	1.0	18.1	2.18	1.831	6.00	0.1039	6.00	4.61	3.65	4.12	4.69	13.5
01	54	1.4	34.6	2.18	1.829	5.28	0.1039	5.63	9.42	7.47	6.88	7.56	25.7
02	108	1.8	69.4	2.18	1.972	7.58	0.1066	6.74	15.36	12.18	10.53	11.32	51.6
03	324	2.2	99.1	1.13	2.088	13.36	0.1088	8.95	16.20	12.84	14.98	16.30	73.8
04	108	−3.4	73.1	2.18	2.012	7.51	0.1074	6.71	16.14	12.80	9.56	10.89	54.4
05	108	−3.4	66.6	2.18	1.965	7.88	0.1065	6.88	14.47	11.47	8.97	9.74	49.6
06	324	3.0	100.0	1.13	2.023	13.74	0.1076	9.08	16.29	12.92	14.58	16.19	74.4
07	324	−1.0	166.8	1.7	2.120	9.58	0.1094	7.58	32.02	25.39	20.97	23.08	124.2
08	972	2.6	202.0	0.76	2.765	14.91	0.1206	9.46	28.18	22.35	30.74	31.91	150.3
09	972	3.4	201.2	0.76	2.094	17.85	0.1089	10.35	28.41	22.53	30.11	32.17	149.7
10	972	3.8	202.1	0.76	2.104	15.51	0.1091	9.65	30.56	24.23	29.72	32.82	150.3
11	972	−1.4	199.8	0.76	2.140	9.52	0.1097	7.56	38.33	30.39	25.20	28.31	148.6
12	972	−1.4	201.9	0.76	2.132	9.55	0.1096	7.57	38.74	30.71	25.70	28.08	150.2
13	972	−1.8	201.4	0.76	2.112	9.54	0.1092	7.57	38.79	30.76	25.24	27.09	149.9
14	972	−2.6	201.9	0.76	2.117	10.71	0.1093	8.02	36.68	29.08	23.99	25.99	150.2
15	972	−2.6	201.4	0.76	2.102	10.42	0.1090	7.91	37.18	29.48	23.38	26.18	149.9
16	972	−2.6	201.9	0.76	2.108	10.44	0.1091	7.92	37.19	29.49	23.52	26.61	150.2
17	972	−2.6	201.8	0.76	2.112	10.61	0.1092	7.98	36.86	29.22	23.85	25.82	150.2
18	972	−2.6	202.2	0.76	2.124	10.36	0.1094	7.88	37.31	29.58	23.60	25.51	150.5
19	324	−3.8	143.6	1.7	2.087	11.49	0.1088	8.30	25.32	20.07	15.76	17.97	106.8

words, the effective width of the distribution becomes smaller in the x direction. However, the ratios of both D_{raw}, based on S_{pc}, and D_{ex}, based on a more complete physics model (MARS), to D_G, also using S_{pc} but with Gaussian measured footprints, are close to 1.

2. Fast beam-loss monitors

Fast BLMs are based on high-purity fused-silica fiber optic (FO) bundles [48,49] as well as small cylindrical fused-silica radiators [50]. Two types of FO bundles are used as BLMs. The first type consists of 61 fibers of 200 μm diameter and forms an effective 3.1 mm^2 circular cross section. The second bundle type is fabricated with seven fibers of 200 μm diameter for an effective circular cross section of 0.34 mm^2. Both FO bundle types are mounted at beam elevation with the downstream ends coupled to photomultiplier tubes (PMTs). The larger cross section bundles are located next to room-temperature undulator vacuum chambers. The smaller bundles are placed within superconducting undulator (SCU) cryostats on either side of the beam pipe [51].

Loss intensity signals observed on one of the SCU fast BLMs at the insertion device, S1 location (ID1) are shown in Fig. 16(a) and compared with PELEGANT simulations of the beam dumps in Fig. 16(b). The PELEGANT simulations consist of the difference in the number of particles remaining with respect to time in units of 3.68 μs turns since rf muting, as described in Sec. III B. These data show qualitative agreement with simulations.

In Fig. 17(a), the measured peak intensity loss times measured from the time of rf muting are determined from the center of the distribution and compared with PELEGANT simulation results in Fig. 17(b). The simulated times since rf mute required to lose 10%, 50%, and 90% of the beam are presented as a function of stored current. Good agreement is seen between the fast BLM data and the PELEGANT 50% simulation. The reduction in time or turns for the appearance of loss signals with current is due to beam loading in the rf cavities. The loss signals correspond to the arrival of the beam on the collimator surface as well as subsequent downstream scattering.

3. Beam position monitors

The peak loss intensity times determined from differentiated TBT BPM sum signals are also included in Fig. 17. A systematic difference of approximately two turns (~7 μs) is observed between the TBT BPMs and the fast BLM data with the fast BLM peaks appearing first. The delay is due to processing latency in the TBT BPM electronics.

4. Imaging of the collimator surfaces during beam dumps

It came as a surprise during the first experiment that beam striking the collimator resulted in easily observed visible light emission even at the lowest current levels

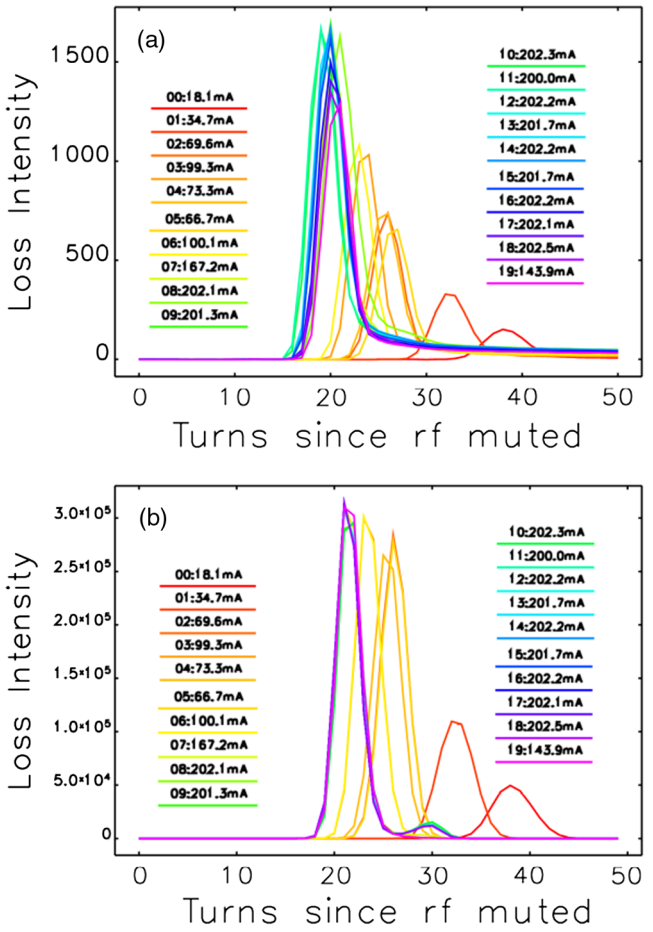

FIG. 16. Loss intensity profiles from (a) ID1 fast BLM and (b) PELEGANT modeling. Both ordinate axes are given in arbitrary units. The leading two-digit numbers in the legend correspond to the beam dump sequence numbers in Table VI.

(approximately 2 mA during the May 2019 study). At low currents, emission is thought to be due to optical transition radiation from the surface, while at high currents, blackbody radiation (BBR) is presumably dominant. During our first experiment, we were limited to maximum currents of 67 mA. Emission images from both studies have been previously reported [19,47]. Visible light emission from beam dumps of 69.4 and 201 mA observed during the second experiment are presented in Fig. 18. Note, the scene shows the first 11 mm at the upstream end of the collimators as do the rest of the images in this section. A digital video recorder (DVR) operating at 30 frames per second was employed to capture these bursts of light. During the second experiment, significantly more linear features were observed in the 65–70 mA range than were seen in the first experiment at similar strike currents; compare Fig. 18(a) with Fig. 5(b) in Ref. [19]. The linear features are believed to be hot ejecta leaving the irradiated zone. Though present at higher current, these linear tracks are better defined (focused) in the 65–70 mA range. The primary mechanical difference between the May 2019 and

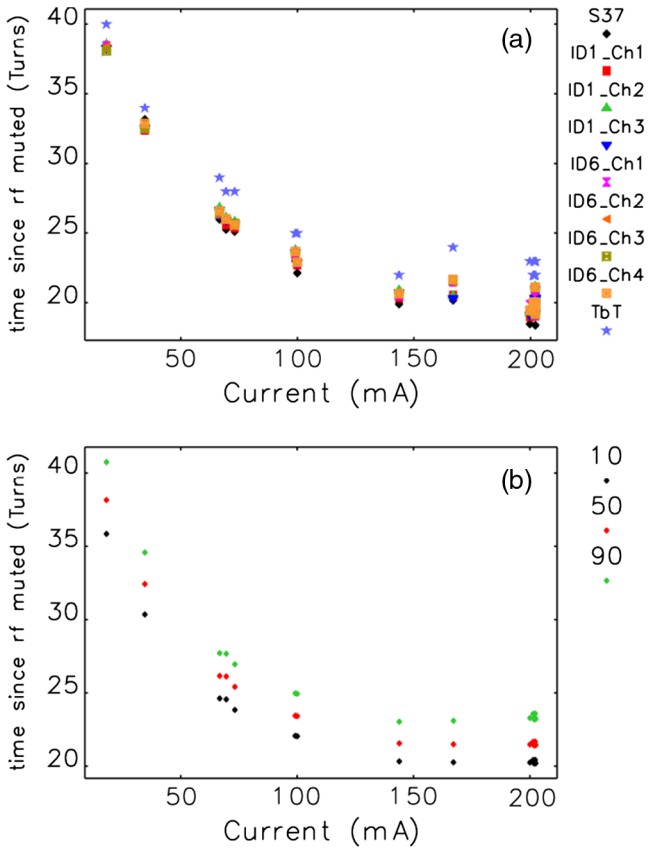

FIG. 17. Comparison of loss signal arrival times determined from (a) the fast BLMs and TBT BPMs and (b) PELEGANT simulations. The fast BLMs are based on high-purity, fused-silica fiber optic bundles; in sector 1 these are labeled ID1_ChM, where M = 1, 2, 3 and in sector 6 labeled ID6_ChN, where N = 1, 2, 3, 4. PELEGANT results are presented for 10, 50, and 90 percent particle loss.

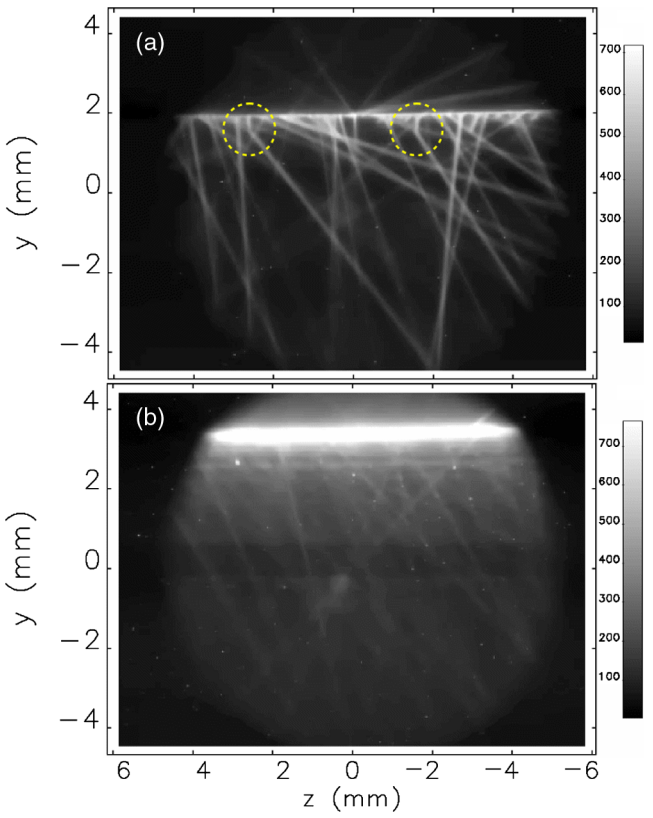

FIG. 18. Visible light emission from beam strikes during experiment 2 at (a) 69.4 mA and (b) 201.2 mA corresponding to SN02 and SN09 in Table VI. Beam is moving from right to left. The yellow dashed circles in (a) are locations where ejecta tracks appear to bend. The horizontal scale is centered on the field of view which is near the upstream end of the collimator. The apex is out of the field of view to the left of the image. The vertical scale is centered at nominal beam elevation ($y = 0$).

January 2020 collimator pieces is surface roughness. In the former case, the average surface roughness was measured to be 2.7 μm, whereas for the latter, the average roughness was found to be 0.45 μm. Perhaps greater roughness leads to wakefield effects that can partially disrupt the beam; in addition, improvements in the control of the vertical emittance were made for the later experiment.

Even at the highest currents, BBR is seen only in one 33-ms DVR frame. The tracks are likely due to a time integration of hot ejecta moving across the scene with widely different trajectories relative to the beam direction. Assuming ejecta velocities are on the order of 1 km/s, the tracks are generated in ~10 μs, much less than the 33-ms video-frame duration.

A few trajectories appear to bend or deflect near the strike zone, as indicated by the dashed circles in Fig. 18(a). In the case of the 69.4-mA beam dump, a peak magnetic field of 0.15 T is present near the bunch; this field, though short in duration (~50 ps, FWHM), may deflect free electrons in the ejecta plasma via magnetic force from the remaining circulating charge. In the case of Fig. 18(b), the lower charge per bunch at 200 mA (see Table VI) means the peak magnetic field is reduced by almost a factor of 3. The surface is illuminated more intensely by the higher current beam dump and the ejecta appear diminished in intensity, both effects make the ejecta harder to distinguish. Nevertheless from the tracks that are visible, no obvious bending is observed.

The depth of focus of the diagnostic camera is 2 mm [47]; therefore, the linear features seen in Fig. 18(a) must be close to the collimator surface. Figure 18(b) shows that while the emission is much brighter at 200 mA, the linear features, though present, are less pronounced perhaps suggesting these features are leaving the depth of field. In these images, beam is moving from right to left.

For the second experiment on the lower collimator test piece, two positions were selected for double strikes and one location received five strikes. Referring to Table VI, these are SN 04 and 05, SN 11 and 12, and SN 14–18, respectively. This was done in order to provide understanding of the survivability of the collimator in real-world operations, where the same location will be struck multiple

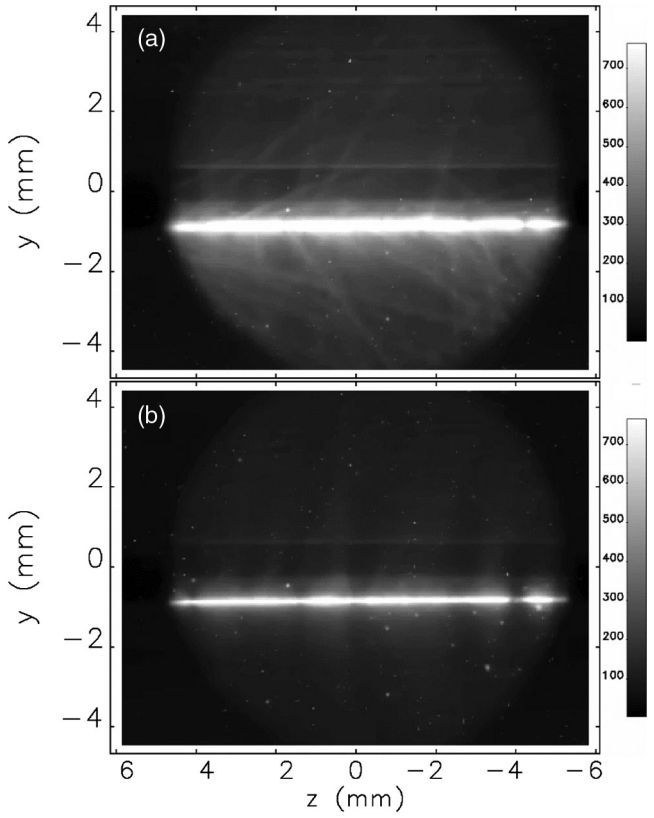

FIG. 19. Emission images at 200 mA from two beam dumps at the same y-offset location; referring to Table VI these strikes are (a) SN11 and (b) SN12. A reduction in light intensity is evident in the second strike.

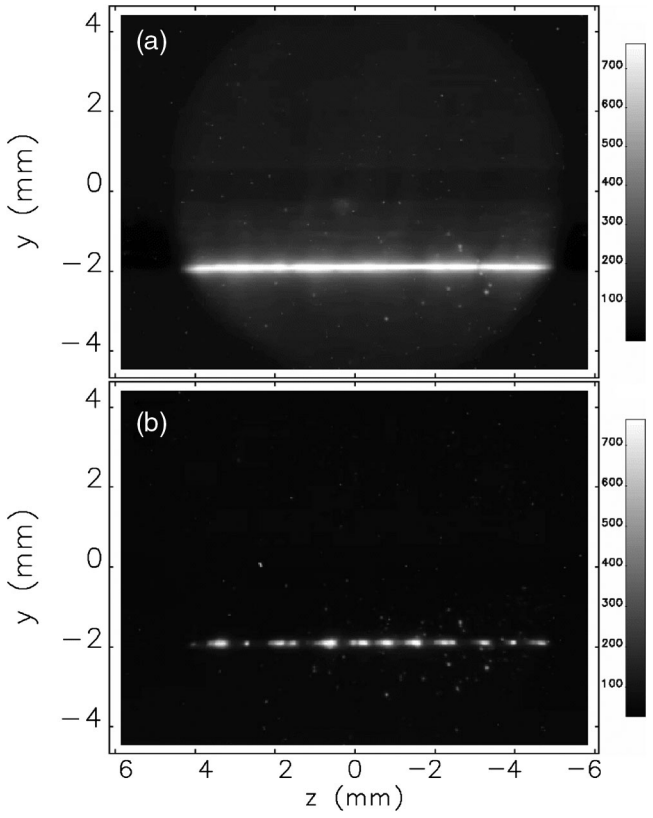

FIG. 20. Emission images at 200 mA from the five-strike case at the same y location. Again referring to Table VI, light intensities from beam strikes (a) SN14 (first) and (b) SN18 (fifth) are shown.

times. Light intensity was observed to drop for later beam dumps at the same vertical offset.

In Fig. 19, the two emission frames from the 200 mA, double strike case (SN11 and 12) are presented. A clear reduction in emission is seen in the second strike. A more dramatic drop in light emission at 200 mA is seen between the first and fifth beam dumps shown in Fig. 20 (SN14 and 18). The number of pixels near saturation (intensity > 700) are roughly the same in the two first-strike cases in Figs. 19(a) and 20(a); however, this region is significantly smaller in the second-strike case, and much smaller for the fifth-strike case. In the five-strike case, the second-strike emission frame (SN15, not shown) displayed a similar reduction in intensity to that shown in Fig. 19(b). The emission from the fifth strike shows strong intensity modulations. The reasons for these variations in emission intensity are not fully understood. Part of the reduction in emission with subsequent dumps at the same y offset may be due to the beam cutting a progressively deeper channel or trench in the collimator material, moving the most intense emission out of the field of view. The region of brightest emission appears to move further downstream.

In addition to imaging the emission of light from the beam strike, the diagnostics camera allowed damage assessment during the experiments. For example, the final image recorded at the end of the May 2019 study is shown in false color in Fig. 21; here color indicates reflected light intensity. This provided immediate confirmation that experimental parameters (i.e., dose) were in line with expectations. Strikes occurred at different elevations by translating the beam with a local bump. The top half was Ti alloy Ti6Al4V, and the lower half of the scraper was Al. Beam current levels are indicated next to the tracks. In this first experiment, beam dumps started at 2 mA; however damage was only visible in the Ti alloy starting at 16 mA and in Al at 32 mA. In both experiments, the field of view (FOV) of the diagnostic camera was 11 mm and is centered at the upstream end of the test pieces.

B. Postirradiation observations

1. Photography of surface postirradiation

Images from the May 2019 experiment showed damage to the titanium alloy test piece was significantly greater than to the aluminum for the same current [19]. Irradiation effects in titanium were observed down to 16 mA; whereas, the minimum current for surface damage in aluminum was 32 mA. This is not surprising because the effect of thermal diffusion in titanium is significantly less than in aluminum.

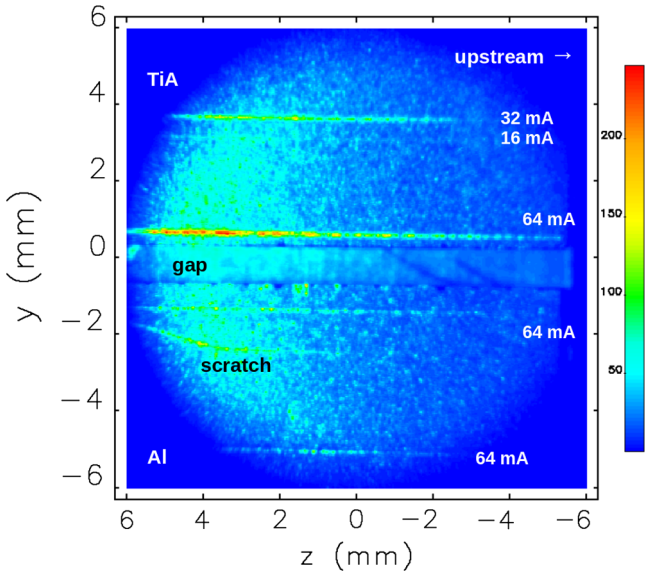

FIG. 21. Last image of the collimator surfaces after the final beam dump of the May 2019 study, shown in false color. The titanium alloy collimator test piece is above the gap and the aluminum piece is below. The field of view is 11 mm. Color indicates reflected light intensity.

One additional complication was that the titanium test piece became activated during the experiment. For these reasons, we decided not to do further testing with titanium.

In early February 2020, after the second experiment, photographs were taken of both aluminum collimator pieces while still attached to the scraper assembly; an example is presented in Fig. 22. For scale, note that the gap between the two collimator pieces is 0.83 mm. The collimator pieces were positioned at $x = -2$ mm; i.e., 2 mm inboard of the horizontal beam centerline prior to dumping the beam via rf muting. The sequence numbers are indicated on the left side of Fig. 22 while targeted current is indicated on the right side (the actual current values are given in Table VI). Locations with more than one sequence number indicate a vertical position struck multiple times. Once the collimator pieces were removed from the scraper body, better resolution images of the irradiation surfaces were obtained.

The collimator test pieces from the January 2020 study were examined with a single-lens reflex camera using a high-magnification macrolens. Different lighting orientations reveal some of the structure of the beam strike damage. Figure 23 presents a photograph of the upper, single-strike collimator piece; the region is indicated by the box in the upper left-hand corner of Fig. 22. Starting from the bottom of Fig. 23, the beam dump currents were 34.6, 69.4, 99.1, 202.0, 100.0, 201.2, and 202.1 mA. The nominal separation between each strike is 0.4 mm.

2. Microscopy of surfaces

Microscopy of all four collimator test pieces from both experiments was carried out using an Olympus BX51M Metallurgical microscope system running StreamMotion software. A set of variable objective lenses provides magnification from 25 to 1000 times. Due to the high magnification, the depth of field is narrow—only a few microns at 500×—therefore, to build an "in-focus" or "flattened" image of the beam strike regions, where depths can vary by over 100 μm, the microscope stage is stepped

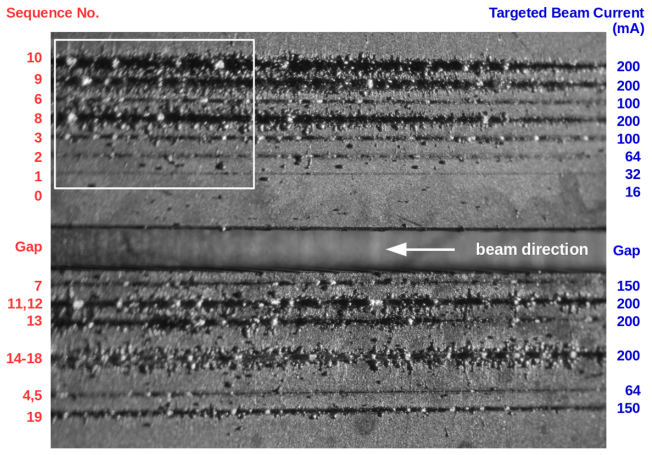

FIG. 22. Photograph of the January 2020 collimator test pieces still attached to the scraper body. Sequence numbers are shown on the left; targeted currents are listed on the right. "Targeted" refers to nominal current we were intending to store before the beam was dumped. The actual currents are given in Table VI. The gap between upper and lower collimator pieces is 0.83 mm. The pieces were positioned at $x = -2$ mm prior to dumping the beam by rf muting.

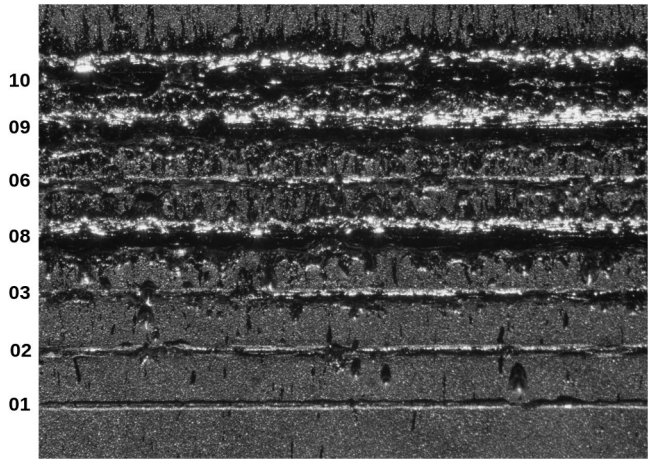

FIG. 23. An enlargement of the boxed region shown in Fig. 22. Sequence numbers, shown on the left, correspond to those given in Table VI; thus, starting from the first visible mark at the bottom are strikes of 34.6, 69.4, 99.1, 202.0, 100.0, 201.2, and 202.1 mA corresponding to sequence numbers 01, 02, 03, 08, 06, 09, and 10, respectively. The vertical separation between each strike position is 0.4 mm. Illumination is from the bottom of the image.

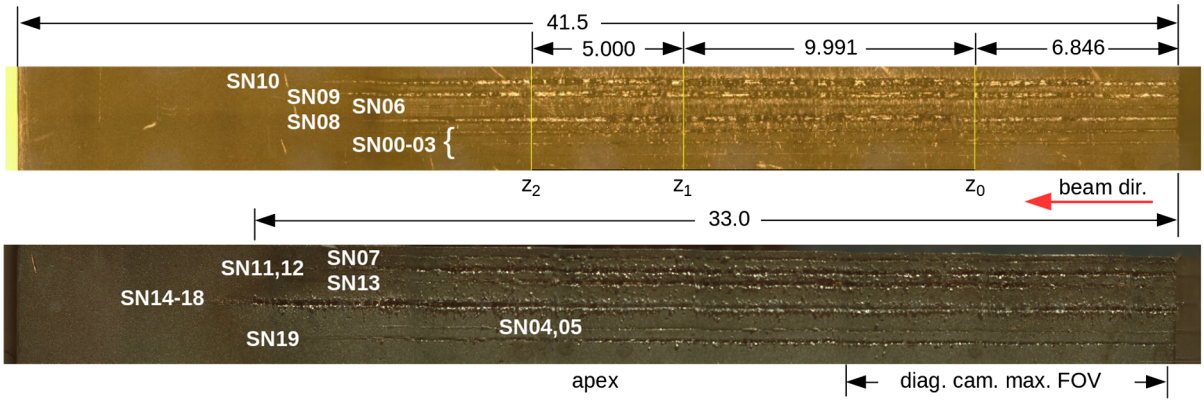

FIG. 24. Overview of the top and bottom collimator test pieces struck by beam dumps recorded at 25× magnification. The top piece was subjected to single-strike beam dumps; the bottom piece received both single and multiple beam dumps at the same vertical offsets. Beam was moving from right to left. Three z locations of interest are indicated on the top image; the apex location is just upstream of the z_2 position. All dimensions are in mm.

vertically. Images are recorded at each step; the regions of each image with the highest spatial frequencies are assembled to form a single frame. Figure 24 shows the regions of top and bottom test pieces struck by the beam; all dimensions are in mm. As mentioned above, the length of the beam-facing surface of each piece is 41.5 mm.

The beam was moving from right to left in the image. Three z locations of interest, designated z_0, z_1, and z_2, are shown in Fig. 24; the collimator apex is located just upstream of z_2. The damaged region appears biased toward the upstream side of the test pieces. One explanation could be the collimators were mounted with a yaw angle (rotation about the y axis). Alternatively, the fact that the collimators were machined with a radius may also play a role. Starting at the apex, as collimator material is removed during the beam dump the strike location must move upstream as the remaining beam moves inboard due to energy loss and positive dispersion.

Single strike.—Microscopy from the May 2019 experiment indicated plastic distortion in the aluminum test piece, and melting in the titanium alloy [19] with maximum currents between 65 and 70 mA. The January 2020 experiment covered a higher range of beam currents. In both experiments, the collimators showed melting in the aluminum above 30 mA; however, in the second study, the area of melting substantially grew as beam current increased from 100 to 200 mA. At 200 mA, the beam left evacuated regions or trenches along its path as material was expelled from the heated volume. In Fig. 25, two adjacent, vertically merged frames show the effects of 100 and 202 mA beam strikes on the top collimator test piece (SN06 and SN08 in Table VI) at the z_0 location indicated in Fig. 24. In multiple strike cases (same y offset), the width of the melt region did not expand; instead, the depth of the trench grew as did the length. Large, thick melt regions are seen as well as much thinner coatings on the surface. The width of the melt zone grew by roughly a factor of 2 from 100 to 202 mA. For comparison, the analysis of simulation data shown in Fig. 6 predict that these variations will begin at lower current, suggesting that the simple approach used in the postsimulation analysis overestimates the extent of melting. A topographical representation of the same

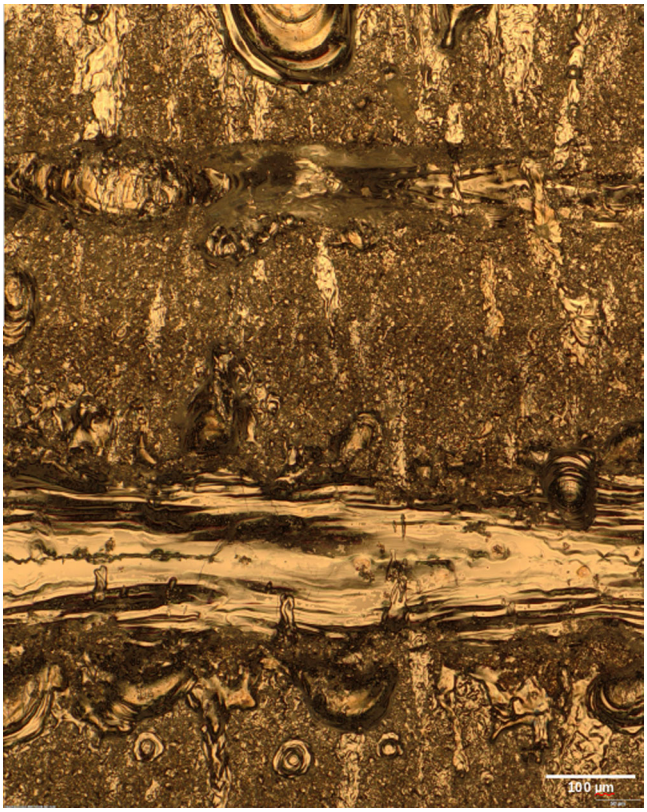

FIG. 25. Adjacent, vertically merged microscopy images of beam strikes SN 06 and 08 (100 mA, upper, and 202 mA, lower), from a 700-μm section of the top collimator at location z_0. The flattened images are recorded at a magnification of 200x.

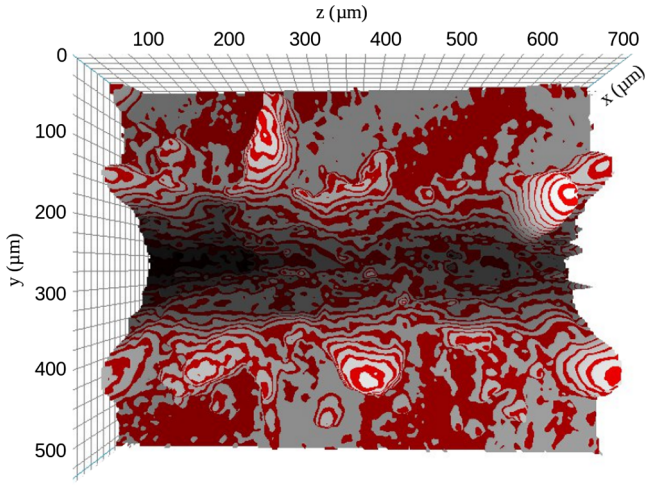

FIG. 26. Anamorphic topological map of beam strike SN 08, 202 mA from the same 700 μm-length section of the top collimator shown in Fig. 25. The increment in the x direction is 2 μm.

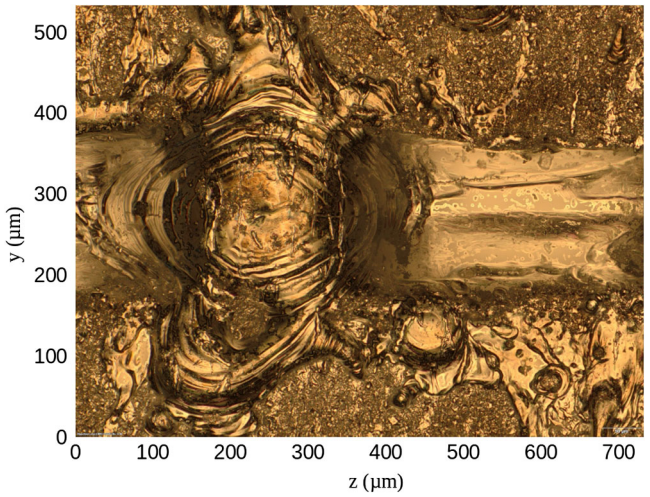

FIG. 28. Flattened image of the SN08, 200 mA beam dump at location z_1. A large variation of trench depth occurs at this position.

SN08, z_0 location is presented in Fig. 26. Each contour line represents a spacing of 2 μm.

Surface profiles in x and y generated every 100 μm in the z direction from the z_0 SN08 position are presented in Fig. 27. Referencing Fig. 26, the lowest profile is taken at $z = 0$ with subsequent profiles corresponding to $z = 100, 200, \ldots, 700$ μm. Such profile data will be used for benchmarking more sophisticated simulations of damage, along the lines outlined in Sec. III C. Even with more sophisticated simulations, comparison with experiments will require careful control and understanding of experimental conditions. This indicates that other factors besides beam current are influencing the outcomes; variation in vertical emittance causing vertical beam size change is one possibility. Vertical emittance changes occur shot to shot, not within a bunch or between bunches and are likely instigated by different vertical beam bumps. An example of transient vertical emittance blowup is shown in Fig. 15 and may be due to an ion instability [52]. From Table VI, 200-mA vertical emittances in the single-strike test piece (SN08-10) were 59% higher than for those in the multi-strike piece (SN11-18).

Variations in the morphology of the damaged regions are also seen over relatively short distances along the strike path; rapid changes in the depth and width are observed. For example in Fig. 28, the flattened, 3D image of beam dump SN08 at the z_1 location appears to show a large melt region overfilling the trench on the downstream (left) side. In Fig. 29, the three depth profiles selected across the strike region presented in Fig. 28 at $z = 0$, 300 and 600 μm confirm the filling of the trench. The location shown in Figs. 28 and 29 is 10.0 mm downstream of the z position displayed in Figs. 25–27 and therefore closer to the collimator apex; this may help to explain the deeper trench

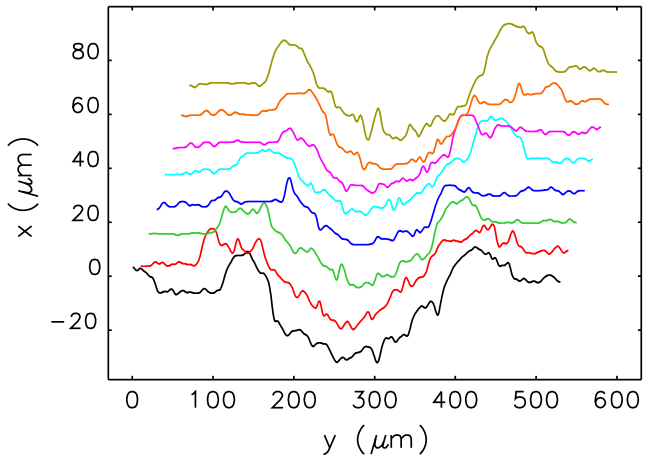

FIG. 27. Surface profiles extracted from the SN08 stack data of Fig. 26 (z_0) in waterfall format. The z separation between profiles is 100 μm.

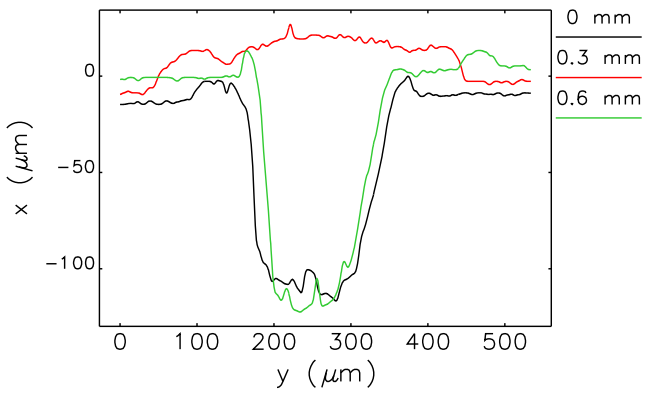

FIG. 29. Surface profiles from the SN08 strike zone of Fig. 28 showing relatively large variation in depth along the trench. Separation between the profiles is 300 μm starting from $z = 0$.

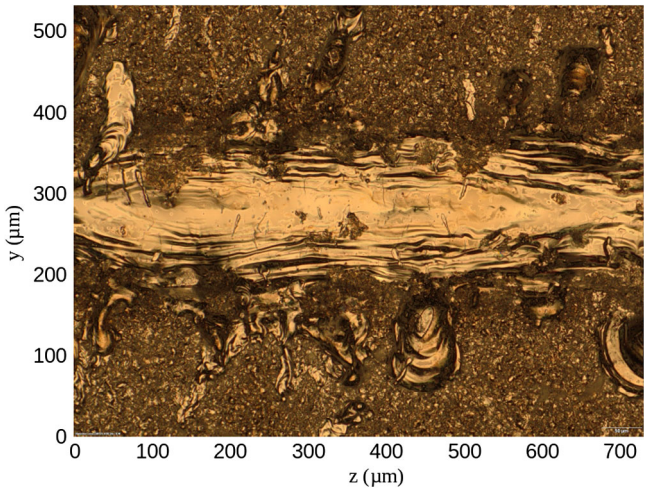

FIG. 30. Flattened image of the SN08, 200-mA, single-strike beam dump at location z_2.

observed there. The HED beam will strike the apex first before striking the upstream location. The microscopy results for 200 mA beam dumps show both trench formation as well as deposition of melted material on both sides of the trench. The z_2 location is 5 mm downstream of z_1, 1.1 mm beyond the nominal apex location. The flattened SN08 z_2 image is presented in Fig. 30. The trench depth at this location is significantly shallower than at z_0 and z_1; this is odd since near the apex is where one would expect the deepest trench depth.

Multiple strike.—The bottom collimator test piece was chosen to receive multiple beam dumps at the same y offset. The five-time strike location (SN14-18) is indicated in Fig. 24 and displays the greatest length of damage, approximately 33 mm. Double strikes at nominal currents of 64 mA (SN 04 and 05) and 200 mA (SN 11 and 12) were also recorded. The flattened image of a five-strike region is shown in Fig. 31.

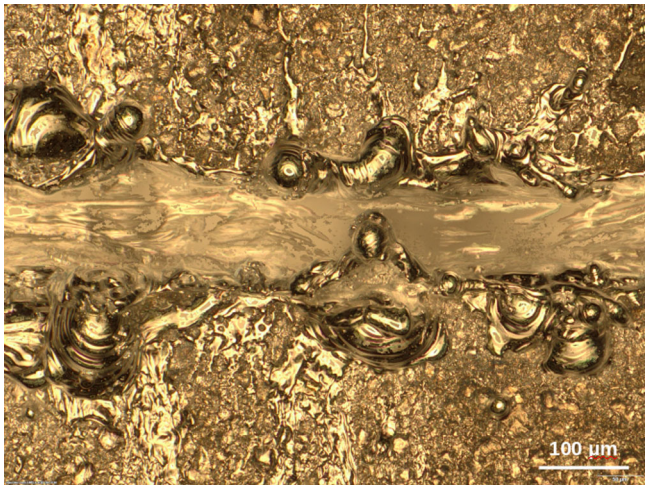

FIG. 31. Flattened image of multiple-strike zone at $y_{\text{off}} = -2.6$ mm; SN 14-18 (Table VI).

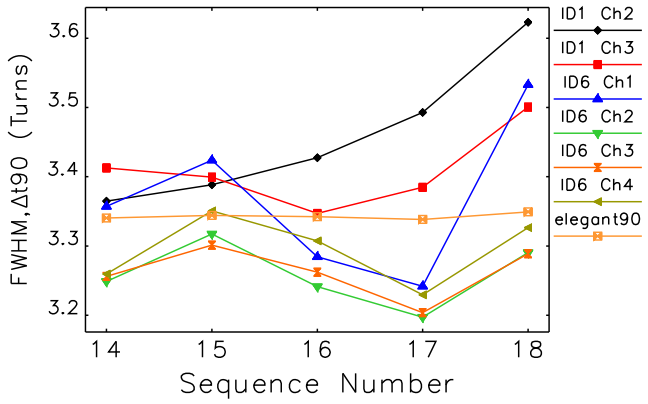

FIG. 32. Five-strike FWHM loss durations taken from ID1 and ID6 fast BLMs compared with PELEGANT 90% loss increment. The BLMs in ID1 are labeled ID1_ChM where $M = 2, 3$; and the BLMs in ID6 are labeled ID6_ChN where $N = 1, 2, 3, 4$.

The maximum trench depth of the five-strike case is significantly greater than for the single strike events; on the other hand, the width, though variable, is typically narrower. For the case shown in Fig. 31 the depth is 200–250 μm. The width of the channel for the five-strike case is approximately 115 μm versus 200–250 μm for the single dump cases on the top piece. Figure 24 indicates the five-strike case creates the longest trench in the bottom test piece. The reduction in light emission shown earlier and the narrow channel suggest the walls cut into the collimator from previous strikes may be interacting with the beam possibly via wakefields, producing loss elsewhere in the SR. (Also, collimator wakefield effects are not included in the PELEGANT modeling at this point; work is ongoing to add this component.) In Fig. 32, loss durations for each of the five-strike cases are compared with the PELEGANT Δt_{90} intervals. Variations are evident in the measured values relative to PELEGANT simulation.

3. Metallurgy

Metallurgical analysis was performed on the aluminum test piece used in the May 2019 experiment. A transverse cross section was cut from the test piece, polished, then prepared with Barker's etch. A comparison of cross sectional regions struck by 33.1 and 67.4-mA beams are presented in Fig. 33. In the figure, regions of plastic flow and partial melt are identified; the beam direction is out of the page.

The size of the affected area (plastic flow or melt) as the current is raised from 33.1 to 67.4 mA is significantly greater than a factor of 2, especially in the partial melt zone. Based on the effects of higher current irradiation during the January 2020 experiment, these cases are viewed as being transitional from no-damage to plastic flow to melting, perhaps accompanied by pockets of vaporization and rapid expulsion of heated material. Table VI shows peak dose

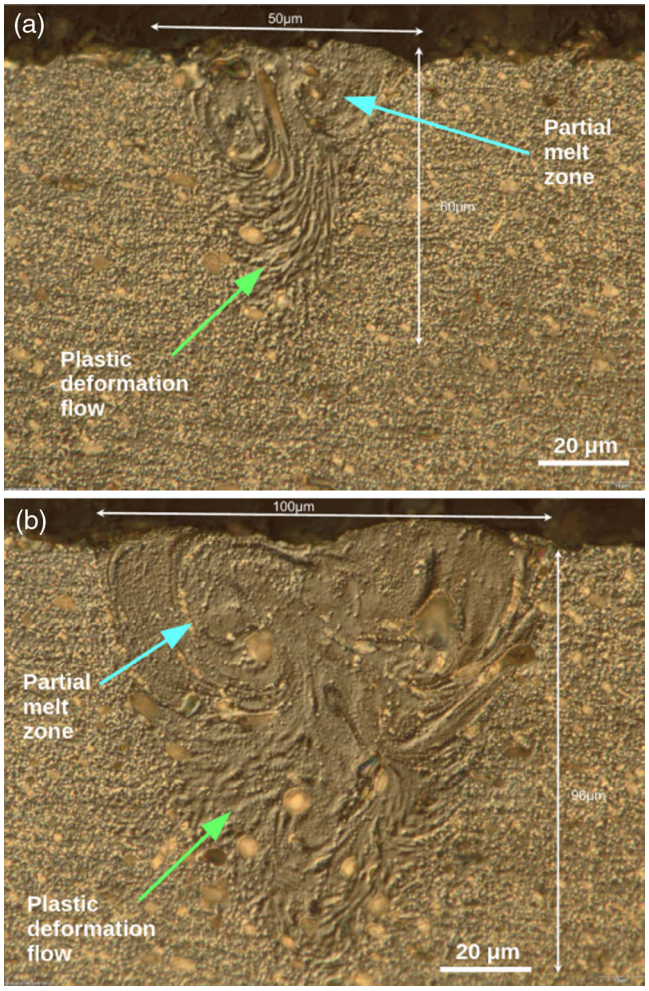

FIG. 33. Polished and etched cross sections of the aluminum test piece from the May 2019 study showing regions struck at (a) 33.1 mA and (b) 67.4 mA.

rates of 30 MGy were attained, a factor of 2 higher than that required for hydrodynamic behavior [38], and approximately 3 times higher than what was achieved in the May 2019 study. The depth of the affected region is important since it will be mechanically weakened during the strike.

TABLE VII. Induced activity of the January 2020 collimator test pieces.

Test piece	Total beam charge (μC)	No. of strikes	^{7}Be (dpm)	^{22}Na (dpm)
Single strike (top)	3.411	8	795	325
Multistrike (bottom)	7.595	12	1535	550

4. Gamma spectroscopy

A metallurgical analysis of the titanium alloy test piece was not conducted due to its activation and the production of mixed waste which would have been generated by cutting and polishing. After the January 2020 experiment, both of the aluminum tests pieces were also found to be activated. Gamma spectroscopy conducted on March 13, 2020 showed the nuclide responsible for the largest count rate was beryllium-7. Be-7 is generated by high-energy events such as spallation or cosmic ray impacts on nitrogen or oxygen in the upper atmosphere. The single-strike collimator piece received a total of 3.411 μC; whereas, the multistrike piece received 7.595 μC. Only a small fraction of the beam energy was deposited in the two pieces. Table VII lists the activity of the two largest contributors, Be-7 and Na-22.

Gamma spectroscopy measurements took place 47 days after irradiation; with a 53.12 day half-life, this implies the initial activity of the Be-7 would have been 1.85 times higher than indicated in the table. Na-22 has a half-life of 2.602 years; therefore its initial activity would have been only slightly higher.

5. Metrology

Table VIII lists the collimator weights before and after irradiation as well as mass loss. The weights of both collimator pieces were measured using a Mettler Toledo XS105 DualRange precision scale. Greater mass loss is noted in the multiple-strike (bottom) piece, which is perhaps expected due to it being struck by more than twice the total charge of the single-strike (top) piece. In addition, the bottom piece experienced a preponderance of the high-current beam aborts. Ejecta observed in images taken with the diagnostic camera shown in Sec. III are clearly part of the mass loss process.

VI. ANALYSIS-POWER DENSITY

Another factor related to beam-induced damage is power density, determined as the energy fluence per unit time. We observed that loss duration tended to decrease with increasing current according to the fast BLMs and TBT BPMs; this effect was also seen in PELEGANT simulations and is readily understood as resulting from rf cavity beam loading. We expect that if the beam is moving faster toward the

TABLE VIII. Weights and weight loss for the January 2020 collimator test pieces.

Test piece	Total beam charge (μC)	No. of strikes	Weight before (mg)	Weight after (mg)	Weight loss (mg)
Single strike	3.411	8	31,785.63	31,785.04	0.59
Multistrike	7.595	12	31,759.29	31,757.83	1.46

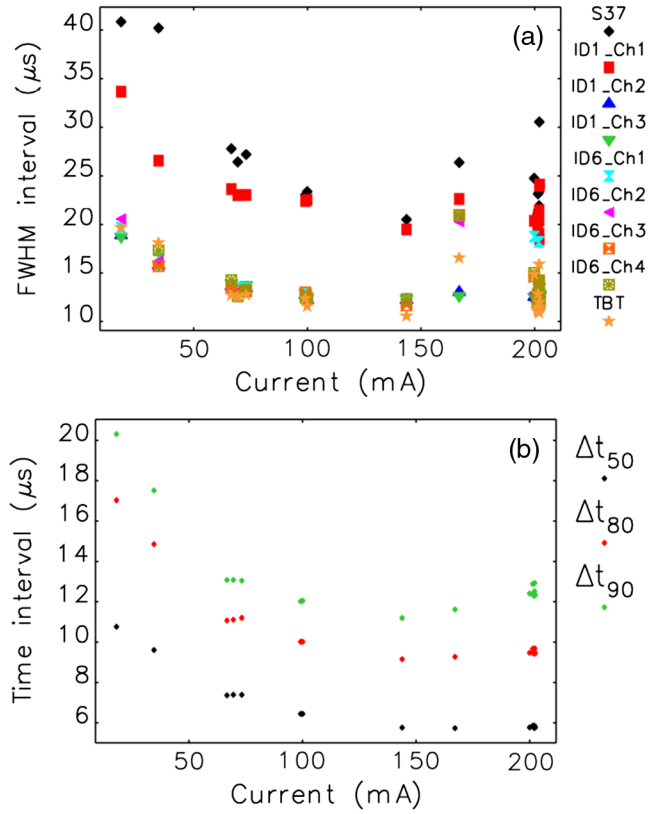

FIG. 34. Comparison of FWHM loss durations for all 20 beam dumps of the second experiment determined from (a) the fast BLMs and TBT BPMs and (b) PELEGANT simulations. PELEGANT results are presented for time required to lose 50, 80, and 90 percent of beam particles. The fast BLMs in ID1 are labeled ID1_ChM where $M = 1, 2, 3$ and those in ID6 are labeled ID6_ChN where $N = 1, 2, 3, 4$. The fast BLM in S37 is simply labeled S37.

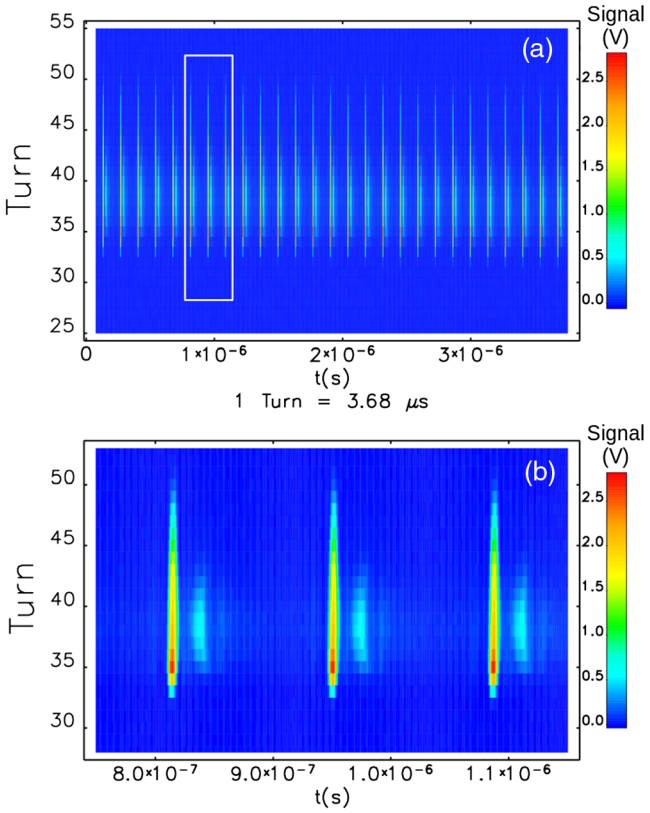

FIG. 35. Contour plots from the ID1 external FO bundle BLM during the 18 mA beam dump. The fill pattern held 27 equally spaced 2.2 nC bunches. The horizontal (fast) axis shows loss signals within a turn, and the vertical (slow) axis shows behavior turn by turn. Part (a) shows loss signals over a full turn on the fast axis; (b) zooms in on losses from three adjacent bunches.

wall with higher current, as seen in Figs. 16 and 17, then assuming the beam maintains a constant cross section, the duration of the loss pulse will decrease and intensity increase. The FWHM duration of loss intensities observed with the fast BLMs and TBT BPMs are presented in Fig. 34(a) and compared with PELEGANT predictions of time intervals required to lose the central 50%, 80%, and 90% of the beam in Fig. 34(b).

The majority of the FWHM data appear to agree most closely with the Δt_{90} PELEGANT predictions; however, fast BLMs in S37, approximately 10 m downstream of the collimator location and in ID1 upstream (US) of the cyrostat both show significantly longer loss intervals. ID1 is the first location in the ring where the beam sees a small-aperture undulator insertion device vacuum chamber after the larger cross sections of the rf zone upstream. Both the S37 and ID1 US radiators are the 61-fiber-bundle BLMs. The difference in FWHM data may be due to saturation; alternatively, charge may continue to circulate in the SR but losses are confined to S37 and ID1 locations. In the low current cases, the charge per bunch is actually greater (2.2 nC); however at high current, though the charge per bunch is smaller (0.77 nC), the bunch signals occur with greater frequency exceeding the response and recovery times of the PMTs. An example of a whole-beam dump event given in Fig. 35 for 18 mA (SN01) shows sufficient time exists for recovery between the loss pulses; here losses detected in the external US ID1 FO bundle in are presented in a contour plot format. The horizontal axis represents signals within a single turn (fast), and the vertical axis exhibits behavior over separate turns (slow). The data sample rate in this case was 2.5 GS s^{-1}.

In Fig. 35, losses are seen to extend over several turns. The loss intensity profiles shown in Fig. 16(a) are derived from similar data collected from one of the internal ID1 FO bundle BLMs. The fact that the full beam current is not lost in a single turn confirms the expectation from simulations that the bunches are clipped or scraped off over multiple turns, lowering the power density seen by the collimators. The faint signals appearing after the main loss pulses are likely due to after-pulsing in the PMT.

Power density can be thought of in terms of average and peak values in the circulating beam as well as in the energy

absorbed per unit time. Power densities associated with average and peak circulating charge may be expressed as

$$P_d = \frac{j_b}{e} E_b \tag{9a}$$

$$P_{d,pk} = \frac{P_d}{N_b} \frac{T_o}{\sqrt{2\pi}\tau_b}, \tag{9b}$$

where e is the electronic charge, τ_b is the rms bunch duration, and E_b is the beam energy. The bunch duration (assume a Gaussian profile) is determined by interpolating [53] between the natural or zero-current value, 18 ps, and the design-current value, 44 ps (15.3 nC) [54]. Circulating power density data are plotted in Fig. 36. While the average circulating power densities increase with beam current, the peak values generally decline as the number of bunches in the higher-current fill patterns increase.

More challenging to ascertain experimentally is the beam cross section as it strikes the collimator; for this, PELEGANT is employed as indicated in Sec. II. Bertarelli defines absorbed power density as absorbed power per unit volume [10]; using this definition, the absorbed power density may be expressed as

$$P_{da} = \dot{D}\rho = S_{pc} \frac{\dot{N}_q \rho}{A_d}, \tag{10}$$

where $\dot{N}_q = I_s(t)/e$, $I_s(t)$ is the time-varying loss current striking the collimator, and A_d is the area of deposition. However, we observe from the BLMs and simulations that the loss duration occurs over more than a single turn. From loss intensity data presented above, we see that $I_s(t)$ is a function of the total current, I. The temporal form of current striking the collimator can be approximated as

$$I_{ns}(t) \approx \frac{eN_q}{\sqrt{2\pi}\tau_b N_b N_t} f_n(t), \tag{11}$$

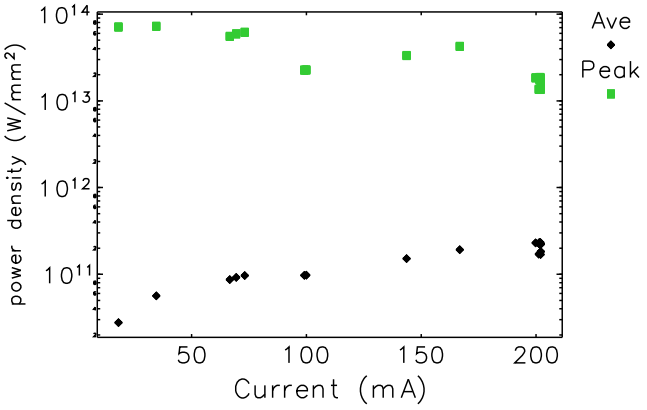

FIG. 36. Average and peak circulating power densities in the 6-GeV electron beam.

where

$$f_n(t) = f_{bn}(t) f_e(t). \tag{12}$$

N_t represents the number of turns required to dump the beam during the strike time $t_s = N_t T_o$ after the beam arrives at the collimator, $f_{bn}(t)$ describes the bunch pattern, and $f_e(t)$ represents the envelope of the loss. For an initial estimate, we express the temporal loss forms as

$$f_{bn}(t) = H\left(t - \frac{nT_o}{N_b}\right) - H\left(t - \left[\frac{nT_o}{N_b} + \sqrt{2\pi}\tau_b\right]\right) \tag{13}$$

and

$$f_e(t) = H(t) - H(t - t_s), \tag{14}$$

where the Heaviside function, $H(\xi) = 0|1$ for $\xi < 0| \geq 0$. The strike time t_s is the FWHM of the loss intensity. In this simple model, the total dose is expressed as

$$D = \int_0^{t_s} \dot{D} dt \approx S_{pc} \sum_{n=0}^{N_b N_t} \frac{N_q}{N_b N_t A_d} f_n = S_{pc} \frac{N_q}{A_d}. \tag{15}$$

During a beam dump, the rf power is muted, and the beam moves inboard due to energy loss and positive dispersion at the collimator location as $\Delta x = \eta_x \Delta p/p$, where $p \approx 6$ GeV/c. As the beam approaches and strikes the collimator apex, charge is shaved off horizontally. Based on the loss intensity and FWHM interval data presented in Figs. 16 and 34, I_s tends to increase with circulating current in a nonlinear manner. The nonlinearity in current can be addressed by adjusting N_t in Eq. (11).

As mentioned in Sec. V, at 200 mA, centroid motion at the collimator is approximately -100 μm/turn. From Table VI, for the 200 mA cases, the circulating horizontal beam size, $\sigma_x \approx 110 \pm 3.4$ μm; thus, with $t_s = 3$ turns or $\approx$11 μs, the beam FWHM x extent at impact should be $\approx$260 μm. This interval is consistent with the PELEGANT loss interval, Δt_{90} shown in Fig. 34(b) and most but not all of the data of Fig. 34(a). Ignoring the effects of wakefields or material loss from the surface of the collimator, we assume the beam is clipped off horizontally at 100 μm per turn (Δx) with no change in the local power density of the remaining circulating charge. The section of the beam striking the collimator is assumed lost and does not recirculate.

We observe from Figs. 9 and 10 that the y profiles are approximately Gaussian but the x profiles are not. This suggests the beam footprint or area on the collimator can be given as $A_d \approx \sqrt{2\pi}\sigma_y l_{dx}$, where l_{dx} is the deposition width. Equating the FWHM$_x$ value shown in the Fig. 10 x profile with l_{dx} (132.1 μm), we see this is 32% larger than the horizontal motion per turn given above. TBT data shows that the centroid motion picks up speed just prior to striking

TABLE IX. Absorbed power density comparing the S_{pc}-derived value for the average of the experimental cases at 200 mA with that from the MARS result and the reference MARS timing-mode bunch for APS-U.

Case	N_b	Q_b (nC)	I_b (mA)	τ_b (ps)	P_{dap} (W cm^{-3})
S_{pc}	972	0.76	201.6	19.0	1.68×10^{11}
MARS	972	0.76	201.6	19.0	1.83×10^{11}
MARS (Ref.)	48	15.3	200.0	44.2	8.39×10^{12}

the collimator. The higher speed would increase the size of the footprint on the collimator; however, the loss duration would further decrease. This implies that the cross section of the beam is growing just prior to striking the collimator. Erosion of the collimator surface may also cause a temporal growth in the strike duration; note that 100 μm is approximately the depth of the trench shown in Fig. 27.

Knowing the beam footprint, current, and beam energy allows calculation of dose in the experiment using the collisional stopping power; this method was employed to calculate D_G and D_{raw} given in Table VI. In the first case, the circulating beam cross was determined knowing the measured beam emittance and lattice functions; in the second case, PELEGANT tracking simulations provided the loss distributions. These calculated dose values are compared with those from MARS simulations, D_{ex} and D_U. PELEGANT-generated loss distribution are necessary to provide estimates of beam footprints on the collimators.

Using the peak dose, the maximum absorbed power density may be expressed simply as

$$P_{\mathrm{dap}} = \frac{D_b \rho}{\sqrt{2\pi}\tau_b}, \tag{16}$$

where D_b is the bunch dose spread over $N_t = 3$ turns. The average of the peak absorbed power densities given by Eq. (16) using the MARS dose for the eleven 200-mA beam dumps are presented in Table IX and compared with those determined from collisional stopping power. Also shown in the table is peak absorbed power density for the 48-bunch 200-mA case for APS-U. The results in Table IX are for a single bunch.

Comparing the absorbed power densities in Table IX with the regions shown in Fig. 1 of Ref. [10] for the individual bunches, the duration is below the chart's deposition time limit (1 ns). The peak absorbed power densities would appear to reside in the elastic and plastic regions.

VII. SUMMARY DISCUSSION

Over the range of currents and bunch patterns selected to conduct these experiments, a diverse set of material behavior has been observed. For example, Fig. 18(a) exhibits numerous ejecta features; whereas images from the first experiment under similar irradiation conditions show none [19]. Surface roughness may play a role when comparing these separate 65–70 mA beam aborts cases in May 2019 and January 2020, suggesting wakefield effects could be involved. Other effects may explain the difference such as trace material composition or improved control of transverse beam dimensions. At 16 mA and below, no damage is detectable on the aluminum collimators. Beginning near 32 mA, plastic deformation and partial melting take place. Above 65 mA, material expulsion is observed; the transverse extent of the damage remains relatively small. At 100 mA and above, the region of damage grows significantly. With 200 mA, the beam strike area is strongly evacuated leaving a clear trench even after a single dump; this is most likely a region of strong hydrodynamic activity as indicated by the dose.

Regarding collimator composition, advanced carbon-based materials such as copper diamond [55,56], carbon fiber [57], and carbon composites [58] may offer better performance than other low-Z, low-density materials such as aluminum. We were given a sample of molybdenum carbide graphite (MoGr) [58] by colleagues at the CERN LHC in September 2019. This was not installed for the January 2020 experiment due to concern of possible graphite dust contamination of the nearby fourth rf cavity in S37. This sample has since been machined into the collimator test piece geometry shown in Fig. 12 in the hope that it may yet be used in future irradiation experiments.

Loss intensities derived from PELEGANT modeling as well as TBT BPMs are global; whereas, observations from loss monitors are local. We might therefore expect temporal loss results to differ somewhat from the disparate methods. In spite of this, we find some agreement between the measurements and simulations with respect to the time required for beam loss to occur and the interval over which a significant fraction of the beam is lost.

Damage is biased toward the upstream side of the collimators; the electron beam will strike the apex first, then necessarily move upstream as the trench begins to form. Alternatively, the upstream bias could be due to a yaw angle in the collimator scraper assembly, meaning a rotation about the y axis.

Improved optical diagnostics would include higher-resolution, higher-speed cameras as well as a system with spectroscopic capabilities to potentially provide temperature information. A digital camera would allow sensor integration down to 10 μs with a triggered start. Depending on BBR optical signal intensity and duration, a gated, intensified charged-coupled device camera could provide 50-ns width images and TBT data.

We have considered just the thermal effects from absorbed energy in the collimator and for now neglected electromagnetic processes that may play a role. The latter effects will be addressed in future work. The large light output at high currents is thought to be predominately BBR. The melting temperature of the T6061 aluminum alloy is

858 and 2345 K for the thin aluminum oxide layer on the surface. In the May 2019 experiment, the oxide layer remained largely intact up to 65 mA; this was not the case in the January 2020 study.

The fact that the struck region forms a trench in a single strike indicates the beam can propagate further downstream as it is lost, i.e., that the beam is not stopped in the collimator. Coupled modeling between particle-matter interaction, hydrodynamic, and beam dynamics codes (multiphysics) is required to adequately address this behavior. Coupling the scattered beam component back to PELEGANT will help us to understand where the remaining energy of the dumped beam will be deposited in the storage ring.

The installation of a vertical fan-out kicker is now being proposed as a method to mitigate the effects of HEDs generated in the collimators during whole-beam loss. The kicker would spread the beam vertically reducing the energy density on the collimator. Simulations have shown that a modest 250-μrad kick can eliminate melting in the aluminum collimator. An experiment has been proposed to test the effectiveness of the vertical fan-out kicker concept.

The work described here has informed the design of the APS-U horizontal collimators in three areas. First, the experiments provide confidence in the simulations carried out thus far in that they predict the conditions are present for damage to take place to the collimators. Second, the effort shows the use of aluminum is favored over other heavier, denser materials; however, additional steps must be taken to protect the collimators. As mentioned above, a vertical fan-out kicker is now under consideration for the APS-U SR. Finally, the work validates the use of a gentle radius (~0.8–1.0 m) on the collimator beam-facing surface to localize the loss.

VIII. CONCLUSION

Two collimator irradiation experiments have been conducted in the APS SR attempting to reproduce expected whole-beam dump conditions in the APS-U by reducing both horizontal and vertical beam sizes. In the first experiment, transitions from solid to plastic/partial-melt states in Al and Ti-alloy target collimators were observed. In the second experiment, 200 mA was attained on aluminum targets, dose exceeded 30 MGy, and transitions to a fully hydrodynamic behavior were observed. Static simulations indicate the APS-U collimator may experience dose levels approaching 150 MGy. An effective reduction in the horizontal extent of deposition as the beam moves inboard with a concomitant increase in dose is a concern with these high-energy-density beams. Beam dynamics predictions by PELEGANT show good agreement with measurements of beam arrival time and temporal pulse compression with current. Because of the superior performance of Al over the Ti alloy as well as its common use, this is the choice now for collimator material. A fan-out kicker system will be employed to deflect beam during whole-beam dumps. Finally, our experiments have provided important data to motivate the benchmarking of ongoing coupled-code multiphysics investigations.

ACKNOWLEDGMENTS

Thanks to R. Soliday and H. Shang for assistance with analysis scripts. We also wish to thank R. Bechtold, R. Diviero, E. Dunn, L. Erwin, G. Moonier, J. Stevens, S. Wesling, and J. Zientek. This research used resources of the Advanced Photon Source, a U.S. Department of Energy (DOE) Office of Science User Facility at Argonne National Laboratory and is based on research supported by the U.S. DOE Office of Science-Basic Energy Sciences, under Contract No. DEAC02-06CH11357.

[1] APS-U Team, Advanced photon source upgrade project final design Report, Technical report, Advanced photon source, Argonne National Laboratory, Report No. APSU-2.01-RPT-003, 2019.

[2] M. Yabashi and H. Tanaka, The next ten years of x-ray science, Nat. Photonics **11**, 12 (2017).

[3] D. Einfeld, M. Plesko, and J. Schaper, A lattice design to reach the theoretical minimum emittance for a storage ring, in *Proceedings of EPAC 1996, Barcelona* (Institute of Physics Publishing, Philadelphia, 1996), https://accelconf.web.cern.ch/e96/PAPERS/WEPG/WEP038G.PDF.

[4] M. Borland *et al.*, The upgrade of the Advanced Photon Source, in *Proceedings of IPAC18, Vancouver, BC, Canada* (JACoW Publishing, Geneva, 2018), pp. 2872–2877, https://accelconf.web.cern.ch/ipac2018/papers/thxgbd1.pdf.

[5] N. V. Mokhov and S. I. Striganov, Fermilab-conf-07/008-ad, AIP Conf. Proc. **896**, 50 (2007).

[6] N. V. Mokhov and F. Cerutti, Beam-material interactions, edited by R. Schmidt, in *Proceedings of the Joint International Accelerator School: Beam Loss and Accelerator Protection* (CERN, Geneva, 2016), Vol. CERN-2016-002, pp. 83–110, https://cds.cern.ch/record/1641418/files/CERN-2016-002.pdf.

[7] M. Plum, Protection related to high-power targets, edited by R. Schmidt, in *Proceedings of the Joint International Accelerator School: Beam Loss and Accelerator Protection* (Ref. [6]), pp. 229–250.

[8] N. Mokhov *et al.*, Beam-induced damage to the Tevatron components and what has been done about it, in the *39th ICFA Adv. Beam Dynamics Workshop High Intensity High Brightness Hadron Beams, HB2006, Tsukuba, 2006*, https://inspirehep.net/conferences/977569.

[9] D. Walz, D. Busick, T. Constant, K. Crook, D. Fryberger, G. Gilbert, J. Jasberg, L. Keller, J. Murray, E. Seppi, and R. Vetterlein, Tests and description of beam containment devices and instrumentation—A new dimension in safety problems, Report No. SLAC-PUB 1223, SLAC, 1973.

[10] A. Bertarelli, Beam-induced damage mechanisms and their calculation, edited by R. Schmidt, in *Proceedings of the Joint International Accelerator School: Beam Loss and Accelerator Protection* (Ref. [6]), pp. 159–227.

[11] N. A. Tahir, J. B. Sancho, A. Shutov, R. Schmidt, and A. R. Piriz, Impact of high energy high intensity proton beams on targets: Case studies for Super Proton Synchrotron and Large Hadron Collider, Phys. Rev. ST Accel. Beams **15**, 051003 (2012).

[12] M. Scapin, L. Peroni, V. Boccone, and F. Cerutti, Effects of high-energy intense multibunches proton beam on materials, Comput. Struct. **141**, 74 (2014).

[13] E. Quaranta, A. Bertarelli, R. Bruce, F. Carra, F. Cerutti, A. Lechner, S. Redaelli, E. Skordis, and P. Gradassi, Modeling of beam-induced damage of the LHC tertiary collimators, Phys. Rev. Accel. Beams **20**, 091002 (2017).

[14] N. A. Tahir, F. Burkart, R. Schmidt, A. Shutov, and A. R. Piriz, Review of hydrodynamic tunneling issues in high power particle accelerators, Nucl. Instrum. Methods Phys. Res., Sect. B **427**, 70 (2018).

[15] Y. Nie, C. Fichera, L. Mettler, F. Carra, R. Schmidt, N. A. Tahir, A. Bertarelli, and D. Wollmann, Simulation of hydrodynamic tunneling induced by high-energy proton beam in copper by coupling computer codes, Phys. Rev. Accel. Beams **22**, 014501 (2019).

[16] T. Bizen *et al.*, Radiation-induced magnetization reversal causing a large flux loss in undulator permanent magnets, Sci. Rep. **6**, 37937 (2016).

[17] Y. Asano, T. Bizen, and X. Marechal, Analyses of the factors for the demagnetization of permanent magnets caused by high-energy electron irradiation, J. Synchrotron Radiat. **16**, 317 (2009).

[18] Y. Suetsugu, High-intensity synchrotron radiation effects, edited by R. Schmidt, in *Proceedings of the Joint International Accelerator School: Beam Loss and Accelerator Protection* (Ref. [6]), pp. 63–82.

[19] J. C. Dooling *et al.*, Studies of beam dumps in candidate horizontal collimator materials for the advanced photon source upgrade storage ring, in *Proceedings of the North American Particle Accelerator Conference (NAPAC'19)* (JACoW Publishing, Lansing, MI, 2019), pp. 128–131, https://jacow.org/napac2019/papers/MOPLM14.pdf.

[20] D. O. Gericke, https://www.journals.elsevier.com/high-energy-density-physics.

[21] R. Abela *et al.*, Design considerations for a Swiss Light Source, in *Proceedings of EPAC 92* (JACoW Publishing, Berlin, Germany 1992), pp. 486–488, https://accelconf.web.cern.ch/e92/PDF/EPAC1992_0486.PDF.

[22] L. Emery and M. Borland, Possible long-term improvements to the Advanced Photon Source, in *Proceedings of the 2003 Particle Accelerator Conference, Portland, OR* (IEEE, New York, 2003), pp. 256–258, https://jacow.org/p03/papers/TOPA014.pdf.

[23] A. Xiao, M. Borland, and C. Yao, On-axis injection scheme for ultralow-emittance light sources, in *Proceedings of the 25th Particle Accelerator Conference, PAC-2013, Pasadena, CA, 2013* (IEEE, New York, 2013), p. 1076, https://jacow.org/PAC2013/papers/WEPSM13.pdf.

[24] M. Borland, J. Dooling, R. Lindberg, and V. Sajaev, Using decoherence to prevent damage to the swap-out dump for the APS ugprade, in *Proceedings of IPAC 2018* (JACoW Publishing, Vancouver, Canada, 2018), pp. 1494–1497, 10.18429/JACoW-IPAC2018-TUPMK004.

[25] J. Dooling and M. Borland, Energy deposition in the APS-U swap-out dump and discussion of whole beam loss, at the *Topical Workshop on Injection and Injection Systems* (Helmholtz-Zentrum Berlin (HZB-Bessy II), Berlin, Germany, 2017), https://indico.cern.ch/event/635514/contributions/2660521/attachments/1514688/2370498/JeffreyDooling-TWIIS.pdf.

[26] M. Borland, ELEGANT: A flexible SDDS-compliant code for accelerator simulation, Technical Report No. LS-287, Advanced Photon Source, 2000.

[27] Y. Wang and M. Borland, Implementation and performance of parallelized ELEGANT, in *Proceedings of the 2007 Particle Accelerator Conference*, http://cern.ch/AccelConf/p07/PAPERS/THPAN095.PDF, pp. 3444–3446.

[28] R. R. Lindberg and A. Blednykh, Modeling of impedance effects for the APS-MBA upgrade, in *Proceedings of IPAC15* (JACoW Publishing, Richmond, VA, 2015), pp. 1825–1827, 10.18429/JACoW-IPAC2015-TUPJE077.

[29] T. Berenc and M. Borland, Modeling rf feedback in ELEGANT for bunch-lengthening studies for the Advanced Photon Source upgrade, in *Proceedings of IPAC 2015* (JACoW Publishing, Richmond, VA, 2015), p. 540, 10.18429/JACoW-IPAC2015-MOPMA006.

[30] M. Tanabashi *et al.* (Particle Data Group), Passage of particles through matter, Phys. Rev. D **98**, 030001 (2018).

[31] Atomic and nuclear properties of aluminum (Al), https://pdg.lbl.gov/2020/AtomicNuclearProperties/HTML/aluminum_Al.html.

[32] Atomic and nuclear properties of tungsten (W), https://pdg.lbl.gov/2020/AtomicNuclearProperties/HTML/tungsten_W.html.

[33] A.-M. Zahra, C. Y. Zahra, G. Jaroma-Weiland, G. Neuer, and W. Lacom, Heat capacities of aluminium alloys, J. Mater. Sci. **30**, 426 (1995).

[34] J. Liu, L. Morrison, G. Waldschmidt, and J. Dooling, Mechanical design and analysis of an electron beam scraper/spoiler at the Advanced Photon Source, in *Proceedings of the MEDSI 2014 Conference* (Australian Light Source, Melbourne, Victoria, 2014), pp. 1–6.

[35] M. Borland, J. Dooling, L. Emery, R. R. Lindberg, V. Sajaev, and Y. P. Sun, Simulation of beam aborts for the Advanced Photon Source to probe material-damage limits for future storage rings, in *Proceedings of the North American Particle Accelerator Conference (NAPAC'19)* (Ref. [23]), pp. 106–109.

[36] NIST ESTAR stopping power and range tables for electrons, https://physics.nist.gov/PhysRefData/Star/Text/ESTAR.html.

[37] J. Safranek, Experimental determination of storage ring optics using orbit response measurements, Nucl. Instrum. Methods Phys. Res., Sect. A **388**, 27 (1997).

[38] D. C. Wilson, R. P. Godwin, J. C. Goldstein, N. V. Mokhov, and C. A. Wingate, Hydrodynamic calculations of 20-TeV beam interactions with the SSC beam dump, in *Proceedings of the 15th Particle Accelerator Conference, PAC-1993, Washington, DC, 1993* (IEEE, New York, 1993), pp. 3090–3093, https://accelconf.web.cern.ch/p93/PDF/PAC1993_3090.PDF.

[39] A. Ferrari, P. R. Sala, A. Fassò, and J. Ranft, FLUKA: A multiparticle transport code, Technical Report No. CERN-2005-010, CERN, 2005.

[40] B. Gladman *et al.*, LS-DYNA keyword users manual—Volume **I**—Version 971, Technical Report No. LSTC, 2007.

[41] ANSYS, ANSYS Autodyn User Manual, Technical report, ANSYS, Release 14.5 2012.

[42] B. Fryxell, K. Olson, P. Ricker, F. X. Timmes, M. Zingale, D. Q. Lamb, P. MacNeice, R. Rosner, J. W. Truran, and H. Tufo, FLASH: An adaptive mesh hydrodynamics code for modeling astrophysical thermonuclear flashes, Astrophys. J. Suppl. Ser. **131**, 273 (2000).

[43] P. Tzeferacos *et al.*, Laboratory evidence of dynamo amplification of magnetic fields in a turbulent plasma, Nat. Commun. 591 (2018).

[44] Y. Lu *et al.*, Modeling hydrodynamics, magnetic fields, and synthetic radiographs for high-energy-density plasma flows in shock-shear targets, Phys. Plasmas **27**, 012303 (2020).

[45] M. Borland, H. Cease, and J. C. Dooling, Use of solid xenon as a beam dump material for 4th-generation storage rings, *Proceedings of the North American Particle Accelerator Conference (NAPAC'19)* (Ref. [19]), pp. 927–930.

[46] Ya. B. Zeldovich and Yu. P. Raizer, *Physics of Shock Waves and High-Temperature Hydrodynamic Phenomena* (Dover, New York, 2002).

[47] J. C. Dooling *et al.*, Diagnostics for collimator irradiation studies in the Advanced Photon Source Storage Ring, in *Proceedings of the 9th International Beam Instrumentation Conference (IBIC'20)* (JACoW Publishing, Santos, Brazil, 2020), 10.18429/JACoW-IBIC2020-TUAO02.

[48] A. S. Fisher, C. I. Clarke, B. T. Jacobson, R. Kadyrov, E. Rodriguez, M. S. Leitner, L. Sapozhnikov, and J. J. Welch, Beam-loss detection for the high-rate superconducting upgrade to the SLAC Linac Coherent Light Source, Phys. Rev. Accel. Beams **23**, 082802 (2020).

[49] J. C. Dooling, W. Berg, L. Emery, and B. X. Yang, Development of a fiber-optic beam-loss position monitor for the Advanced Photon Source Storage Ring, in *Proceedings of the 23rd Particle Accelerator Conference, Vancouver, Canada, 2009* (IEEE, Piscataway, NJ, 2009), pp. 3438–3440, https://jacow.org/PAC2009/papers/TH5RFP003.pdf.

[50] A. Pietryla, W. Berg, and R. Merl, A Cerenkov radiation detection system for the Advanced Photon Source Storage Ring, in *Proceedings of the 19th Particle Accelerator Conference, Chicago, IL, 2001* (IEEE, Piscataway, NJ, 2001), pp. 1622–1624, https://jacow.org/p01/papers/TPAH304.pdf.

[51] J. C. Dooling, K. C. Harkay, V. Sajaev, and H. Shang, Operational experience with fast fiber-optic beam-loss monitors for the Advanced Photon Source Storage Ring superconducting undulators, in *Proceedings of the North American Particle Accelerator Conference (NAPAC16)* (JACoW Publishing, Chicago, IL, 2016), pp. 28–31, 10.18429/JACoW-NAPAC2016-MOA3CO04.

[52] J. R. Calvey *et al.*, Advances in understanding of ion effects in electron storage rings, in *Proceedings of the 12th International Particle Accelerator Conference (IPAC'21)* (JACoW Publishing, Campinas, Brazil, 2021), pp. 1267–1272, 10.18429/JACoW-IPAC2021-TUXA01.

[53] T. Ieiri, Measurement of bunch length based on beam spectrum in the KEKB, in *Proceedings of the 7th European Particle Accelerator Conference (EPAC'00), Vienna, 2000* (EPS, Geneva, 2000), pp. 1735–1737, https://jacow.org/e00/papers/WEP5A14.pdf.

[54] H. Bizek, The Advanced Photon Source list of parameters, Technical Report No. ANL/APS/TB-26, Advanced Photon Source, 1996.

[55] M. Borg, A. Bertarelli, F. Carra, P. Gradassi, J. Guardia-Valenzuela, M. Guinchard, G. Arnau Izquierdo, P. Mollicone, O. Sacristan-de-Frutos, and N. Sammut, Thermostructural characterization and structural elastic property optimization of novel high luminosity LHC collimation materials at CERN, Phys. Rev. Accel. Beams **21**, 031001 (2018).

[56] G. Gobbi, A. Bertarelli, F. Carra, J. Guardia-Valenzuela, and S. Redaelli, Novel LHC collimator materials: High-energy hadron beam impact tests and nondestructive postirradiation examination, Mech. Adv. Mater. Struct. **27**, 1518 (2020).

[57] N. Simos *et al.*, Radiation damage of a two-dimensional carbon fiber composite (CFC), Carbon Trends **3**, 100028 (2021).

[58] J. Guardia-Valenzuela, A. Bertarelli, F. Carra, N. Mariani, S. Bizzaro, and R. Arenal, Development and properties of high thermal conductivity molybdenum carbide-graphite composites, Carbon **135**, 72 (2018).